



# Outflow from Outer-arm Starburst in a Grazing Collision between Galaxies

Michele Kaufman<sup>1,8</sup> , Bruce G. Elmegreen<sup>2</sup> , Morten Andersen<sup>3</sup> , Debra Meloy Elmegreen<sup>4</sup> , Curtis Struck<sup>5</sup> ,  
Frédéric Bournaud<sup>6</sup> , Elias Brinks<sup>7</sup> , and James C. McGarry<sup>7</sup>

<sup>1</sup> 110 Westchester Road, Newton, MA 02458, USA; [kaufmanrallis@icloud.com](mailto:kaufmanrallis@icloud.com)

<sup>2</sup> IBM Research Division, T.J. Watson Research Center, 1101 Kitchawan Road, Yorktown Heights, NY 10598, USA; [bge@us.ibm.com](mailto:bge@us.ibm.com)

<sup>3</sup> Gemini Observatory, NSF's National Optical-Infrared Astronomy Research Laboratory Casilla 603, La Serena, Chile; [manderse@gemini.edu](mailto:manderse@gemini.edu)

<sup>4</sup> Department of Physics & Astronomy, Vassar College, Poughkeepsie, NY 12604, USA; [elmegreen@vassar.edu](mailto:elmegreen@vassar.edu)

<sup>5</sup> Department of Physics & Astronomy, Iowa State University, Ames, IA 50011, USA; [curt@iastate.edu](mailto:curt@iastate.edu)

<sup>6</sup> Laboratoire AIM-Paris-Saclay, CEA/DSM-CNRS-Université Paris Diderot, Irfu/Service d'Astrophysique, CEA Saclay, Orme des Merisiers, F-91191 Gif sur Yvette, France; [frederic.bournaud@gmail.com](mailto:frederic.bournaud@gmail.com)

<sup>7</sup> University of Hertfordshire, Centre for Astrophysics Research, College Lane, Hatfield AL10 9AB, UK; [e.brinks@herts.ac.uk](mailto:e.brinks@herts.ac.uk), [jcmcgarry@virginmedia.com](mailto:jcmcgarry@virginmedia.com)

Received 2019 January 28; revised 2020 February 25; accepted 2020 February 29; published 2020 March 30

## Abstract

Gemini NIFS *K*-band spectra and Atacama Large Millimeter/submillimeter Array  $^{12}\text{CO } J = 1 \rightarrow 0$ ,  $\text{HCO}^+$ , and 100 GHz continuum observations are used to study a bright starburst clump on an outer arm of the interacting galaxy NGC 2207. This clump emits 23% of the total  $24 \mu\text{m}$  flux of the galaxy pair and has an optically opaque dust cone extending out of its 170 pc core. The measured CO accounts for the dark cone extinction if almost all the gas and dust there are in front of the star clusters. An associated approaching CO outflow has  $v_z \sim 16 \text{ km s}^{-1}$ , an estimated molecular mass  $8 \times 10^6 M_\odot$ , and rises to heights  $\sim 0.9 \text{ kpc}$ . A receding CO outflow on the far side with  $v_z \sim 28 \text{ km s}^{-1}$  is less extensive. The observed star formation in the core over 10 Myr can supply the dark cone kinetic energy of roughly  $2 \times 10^{52} \text{ erg}$  via supernovae and stellar winds. Other signs of intense activity are a variable radio continuum, suggesting an embedded supernova or other outburst; X-ray emission possibly from an X-ray binary or intermediate-mass black hole, depending on the extinction; and  $\text{Br}\gamma$  and  $\text{He I}$  lines with  $82 \text{ km s}^{-1}$  line widths and fluxes consistent with excitation by embedded O-type stars. According to previous models, the retrograde encounter suffered by NGC 2207 caused the loss of angular momentum. This compressed its outer disk. We suggest that the resulting inward crashing stream hit a massive HI clump on the preexisting spiral arm and triggered the observed starburst.

*Unified Astronomy Thesaurus concepts:* [Interacting galaxies \(802\)](#); [Starburst galaxies \(1570\)](#); [Interstellar medium \(847\)](#); [Interstellar molecules \(849\)](#)

## 1. Introduction

The spiral galaxies IC 2163 and NGC 2207 are involved in a grazing encounter (Elmegreen et al. 1995a, 1995b; Struck et al. 2005). A prominent starburst region called Feature i by Elmegreen et al. (2000) lies in an outer arm of NGC 2207 on its anticompanion side. Feature i is the most luminous  $8 \mu\text{m}$ ,  $24 \mu\text{m}$ ,  $70 \mu\text{m}$ ,  $\text{H}\alpha$ , and radio continuum source in NGC 2207/IC 2163 (Elmegreen et al. 2001, 2006; Kaufman et al. 2012) and accounts for 23% of the total  $24 \mu\text{m}$  emission from the galaxy pair (Elmegreen et al. 2006, 2016). The star formation rate (SFR) of Feature i is  $1.6 M_\odot \text{ yr}^{-1}$  (Smith et al. 2014; Elmegreen et al. 2016), which is enormous for a clump not in a galactic nucleus or a galaxy merger, or in the expanding ring of a collisional ring galaxy. The gas ( $\text{H}_2 + \text{HI}$ ) depletion time of Feature i,  $\sim 100 \text{ Myr}$  (Elmegreen et al. 2016), lies in the range of starburst galaxies (see, for example, the Kennicutt–Schmidt diagram in Bigiel et al. 2008).

Comparable in SFR to the brightest star-forming clump in the overlap part of the Antennae galaxies (Smith et al. 2014), Feature i has the seventh highest SFR among the set of 1700 star-forming complexes in interacting galaxies or normal spirals measured by Smith et al. (2016) with a 1 kpc aperture. Because of its high SFR and location on an outer arm, Smith et al. (2014) include Feature i in their study of hinge clumps. Hinge clumps are regions of multiple converging flows, usually

involving a tidal arm produced in a prograde encounter. In contrast, the encounter suffered by NGC 2207 was retrograde and somewhat out of plane (Elmegreen et al. 1995a; Struck et al. 2005). We shall consider how such an encounter may have led to the formation of Feature i.

The most striking property of Feature i is a large optically opaque, conically shaped dust cloud extending a projected  $3''$  ( $\sim 500 \text{ pc}$ ) from the center of its  $\sim 1''$  core. This structure suggests that there is a large-scale outflow of gas inclined with respect to the disk at Feature i and thus feedback from the starburst. We present new observations of Feature i in  $^{12}\text{CO } J = 1 \rightarrow 0$ ,  $\text{HCO}^+$ , and millimeter-wave continuum (in the range 88–106 GHz) from the Atacama Large Millimeter Array (ALMA) and *K*-band spectrometry from Gemini NIFS. We then combine these observations with previous radio to X-ray data in order to study the outflow and determine the energy source(s) in this intriguing, partly obscured star-forming region.

NGC 2207/IC 2163 contain massive ( $10^8$ – $10^9 M_\odot$ ) HI clouds that do not coincide with the brighter star-forming knots in these galaxies (Elmegreen et al. 1993, 1995b). The massive HI clouds are located in large areas of these galaxies that have high velocity dispersion ( $30$ – $50 \text{ km s}^{-1}$ ) in the HI gas. Similar massive HI clouds in regions with high HI velocity dispersion are found in other interacting galaxies in an early stage of post-encounter evolution, for example, Arp 82 (Kaufman et al. 1997), Arp 84 (Kaufman et al. 1999), and the NGC 5774/75 pair (Irwin 1994). Presumably, the galaxy encounters increased the HI velocity dispersion and thus the gravitational Jeans mass of the

<sup>8</sup> Corresponding author.

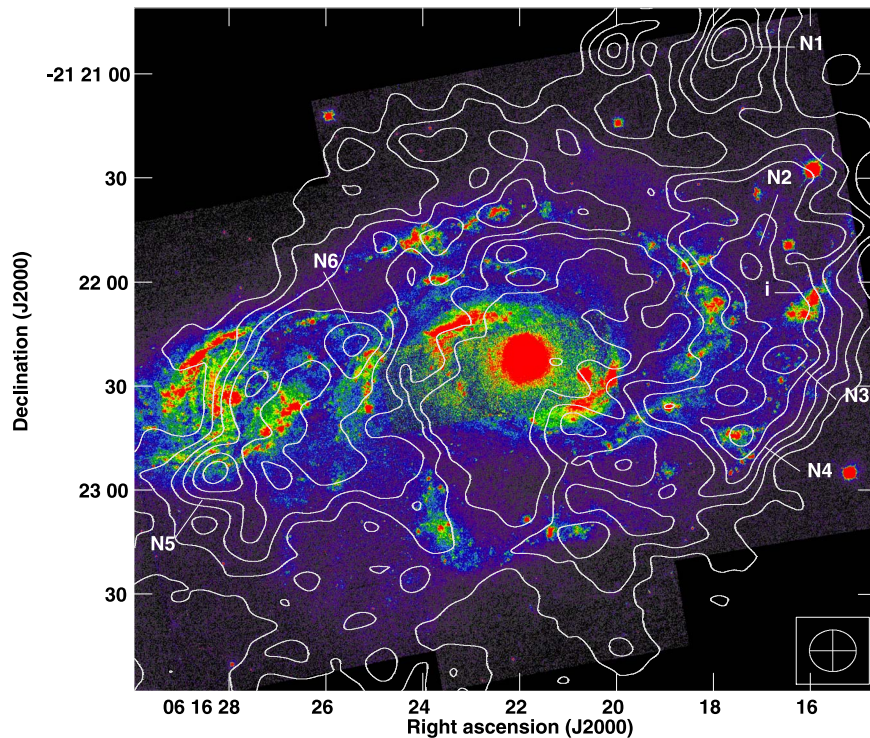


**Figure 1.** H I line-of-sight column density contours of NGC 2207 overlaid on a color-coded Hubble Space Telescope (HST *B*) image (Elmegreen et al. 2000) with contours at 10, 15, 20, 25, 30, and  $35 M_{\odot} \text{pc}^{-2}$ . Part of the companion IC 2163 is to the left. Feature *i*, on an outer arm of NGC 2207 on the anticompanion side, is labeled *i*. The six massive H I clouds in NGC 2207 are labeled N1 through N6. The beam symbol represents the H I beam.

largest clouds in these galaxies (Elmegreen et al. 1993; Wetzstein et al. 2007). Although Feature *i* does not presently correspond to a massive H I cloud, it is similar to massive H I clouds in the mass of its cold gas,  $\sim 2 \times 10^8 M_{\odot}$  (Elmegreen et al. 2016); overall size,  $1.4 \times 1.7 \text{ kpc}$  (Kaufman et al. 2012); and location in a region with high H I velocity dispersion. Feature *i* may illustrate what a massive H I cloud could become if an outburst of star formation were triggered in it.

From the NASA/IPAC Extragalactic Database (NED), we adopt a distance of  $35 \pm 2.5 \text{ Mpc}$  for NGC 2207 with a Hubble constant  $H = 73 \text{ km s}^{-1} \text{ Mpc}^{-1}$  and corrected for infall toward Virgo. Then,  $1'' = 170 \text{ pc}$ . Our velocities are heliocentric and use the optical definition of the nonrelativistic Doppler shift.

Rupke et al. (2010) measure  $[\text{O}/\text{H}] = 8.874$  in Feature *i*, so metallicity close to solar. We therefore adopt the standard value  $X_{\text{CO}} = (1.8 \pm 0.3) \times 10^{20} \text{ H}_2 \text{ cm}^{-2} (\text{K km s}^{-1})^{-1}$  for normal galaxies (Dame et al. 2001) to convert the CO emission to molecular mass. In Section 4, we comment on whether a reduced value of  $X_{\text{CO}}$  is appropriate for Feature *i*.

An overview of Feature *i* from previous observations is presented in Section 2, and a description of our new data in Section 3. Because star formation in parts of Feature *i* may be hidden by heavy obscuration, we investigate the level of extinction and the dust distribution in Section 4. The amount of extinction at the detected X-ray source in Feature *i* is relevant to whether this source could be an intermediate-mass black hole. Section 5 identifies the two main CO components of Feature *i*. In Section 6, we focus on the star-forming core of Feature *i* and compare its properties in the broadband optical, CO,  $\text{HCO}^+$ , and near-infrared emission lines, 100 GHz continuum, and radio continuum. We discuss the internal kinematics of the cold gas, the gas velocity dispersion, possible outflows, and the three-dimensional orientation of the latter in Section 7. In Section 8,

we hypothesize a possible origin for Feature *i*, and Section 9 summarizes our conclusions.

## 2. Overview and Previous Results

The location of Feature *i* in NGC 2207 (at a distance of 15 kpc from the NGC 2207 nucleus) and the locations of the six massive H I clouds (N1–N6) are marked in Figure 1, which displays the Hubble Space Telescope (HST) *B* image overlaid with the H I column density contours of NGC 2207 (Elmegreen et al. 1995b, 2000). The H I velocity of Feature *i* is consistent with that of the surrounding H I in the NGC 2207 disk; thus, it is likely that Feature *i* formed in the disk. Table 1 lists previous observations from radio to X-rays of Feature *i*, along with the values of the FWHM of the point-spread function (PSF) and for the radio and millimeter-wave observations, the rms noise  $\sigma_{\text{eff}}$  at the location of Feature *i* after correcting for primary-beam attenuation. Important components of Feature *i* are its core, the central star complex, the cluster arcs, the opaque dust cone, and the red V-shaped dust structure. These are marked in Figure 2. Their relevant properties are summarized below.

### 2.1. Radio Continuum and $8 \mu\text{m}$ : The Core and the Extended Emission

In the  $\lambda 6 \text{ cm}$  radio continuum images from NSF’s Karl G. Jansky Very Large Array (VLA)<sup>9</sup> and in the Spitzer  $8 \mu\text{m}$  image, Feature *i* consists of a bright core with FWHM  $\sim 1''$  ( $=170 \text{ pc}$ ) embedded in a region of extended emission of dimension  $8'' \times 9''6$  ( $=1.4 \times 1.7 \text{ kpc}$ ); see Figure 12 in Kaufman et al. (2012). The location of maximum surface

<sup>9</sup> The National Radio Astronomy Observatory is a facility of the National Science Foundation operated under cooperative agreement by Associated Universities, Inc.

**Table 1**  
Some Previous Observations of Feature i<sup>a</sup>

Data Set	Date Observed (YYYY-mm-dd)	PSF (HPBW, BPA)	Noise $\sigma_{\text{eff}}$ (mJy beam <sup>-1</sup> )	References
(1)	(2)	(3)	(4)	(5)
Spectral Line:				
VLA H I	1990 Oct 11	13''.5 × 12''.0, 90°	0.73	1
ALMA <sup>12</sup> CO $J = 1 \rightarrow 0$	2014 Apr 3	2''.00 × 1''.52, -68°5	4.4	2, 3
Lowell H $\alpha$	1999 Oct 6	4''.2 × 3''.6	...	4
Continuum:				
VLA 1.49 GHz	1986 Mar 18	1''.92 × 1''.11, 9°	0.19	5
VLA 1.40 GHz	1990 Oct 11	10''.1 × 6''.5, 90°	0.37	1
VLA 4.86 GHz	1986 Aug 16	1''.93 × 1''.04, 169°	0.07	5
VLA 4.86 GHz	2001 Apr 14	2''.47 × 1''.30, 8°	0.013	6
Spitzer 24 $\mu$ m	2005 Mar 11	6''	...	7, 2
Spitzer 8 $\mu$ m	2005 Feb 22	2''.4	...	7
HST <i>UBVI</i>	1996 May 25	0''.18	...	8, 3
XMM-Newton UVM2	2005 Aug 31	1''.8	...	6
Galex NUV	...	5''	...	9
Chandra	2010–2013	1''	...	10

#### Notes.

<sup>a</sup> For the radio and millimeter-wave observations,  $\sigma_{\text{eff}}$  is the rms noise at Feature i after correcting for primary-beam attenuation. It has units of mJy beam<sup>-1</sup> per channel for the spectral-line observations mJy/beam and for the continuum observations.

**References.** (1) Elmegreen et al. (1995b), (2) Elmegreen et al. (2016), (3) Elmegreen et al. (2017), (4) Elmegreen et al. (2001), (5) Vila et al. (1990), (6) Kaufman et al. (2012), (7) Elmegreen et al. (2006), (8) Elmegreen et al. (2000), (9) Smith et al. (2014), (10) Mineo et al. (2014).

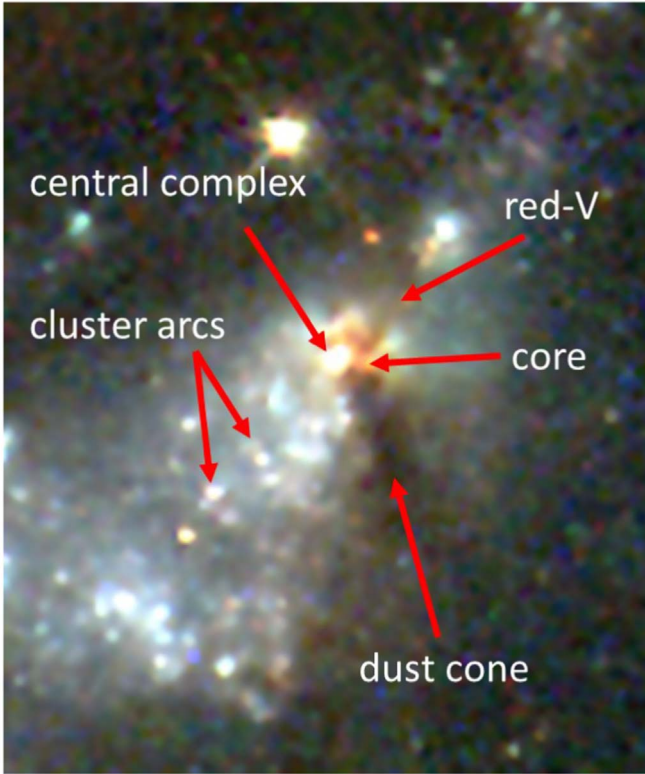


**Figure 2.** HST color composite image of Feature i and surroundings with the following structures labeled: the central star complex, the concentric arcs of smaller clusters, the optically opaque dust cone extending 3'' to the southwest of the central star complex, and the red V-shaped dust structure opening to the north. The field displayed is 15'' × 18''. The  $\sim 1''$  core of Feature i contains the vertex of the red V, the center of the central star complex, the apex of the dark dust cone, and the radio continuum peak. Within the uncertainties, the vertex of the red V coincides with the radio continuum peak and the Spitzer 8  $\mu$ m emission peak. The possible ULX detected with Chandra lies at, or close to, the radio continuum peak.

brightness in the radio continuum is at R.A., decl. (J2000) = 06 16 15.865, -21 22 02.77 (Vila et al. 1990) with an uncertainty of 0''.1–0''.2 (10% of the half-power beam width, HPBW). We shall use this as the point from which relative positions are quoted throughout this paper.

Scaled-array VLA observations show that both the core and the surrounding region are dominated by nonthermal emission at  $\lambda 20$  cm and  $\lambda 6$  cm. With a 7''.5 × 7''.5 aperture, Vila et al. (1990) measure flux densities  $S_\nu(20 \text{ cm}) = 10.3$  mJy and  $S_\nu(6 \text{ cm}) = 3.4$  mJy and a spectral index  $\alpha = -0.9$  (where  $S_\nu \propto \nu^\alpha$ ). For the  $\sim 1''$  core, their Gaussian fit gives  $S_\nu(20 \text{ cm}) = 3.4$  mJy,  $S_\nu(6 \text{ cm}) = 1.4$  mJy, and  $\alpha = -0.7$ . A near doubling of the  $\lambda 6$  cm flux density of the Feature i core between 1986 and 2001 (Kaufman et al. 2012) is evidence of a possible radio supernova in the core.

#### 2.2. Optical: Central Star Complex, Cluster Arcs, Opaque Dust Cone, and Red V-shaped Dust Structure

In the HST *B* image, the only star complex detected in the core of Feature i has a mass of  $2 \times 10^6 M_\odot$ , an age of 0.6 Myr (Elmegreen et al. 2017), and a size of 0''.6 × 0''.4 (100 × 70 pc) with major axis at a position angle (PA) of  $-45^\circ$ . The center of this star complex is 0''.4 east, 0''.4 south of the radio peak; the uncertainties in position are  $\sim 0''.25$  in the absolute astrometry of the HST image and 0''.1–0''.2 for the radio continuum peak. This central star complex is surrounded by concentric arcs of 13 smaller star complexes that lie within the radio and 8  $\mu$ m region of extended emission (Elmegreen et al. 2000, 2017). These range in age from 0.6 to 60 Myr with an average age of 7.9 Myr and an average mass of  $1.6 \times 10^5 M_\odot$ . There is no obvious pattern of cluster age with distance from the radio peak in the core.

The central star complex together with a reddish dusty region on its western edge is near the apex of the optically opaque dust cone which extends to the southwest for a projected length of

**Table 2**  
New ALMA Spectral-line Observations of Feature i

Parameter	$^{12}\text{CO } J = 1 \rightarrow 0$	HCN	HCN	$\text{HCO}^+$	$\text{HCO}^+$
Date observed	2015 May 15	2014 Aug 30	2015 Jun 7	2014 Aug 30	2015 Jun 7
$uv$ coverage ( $k\lambda$ )	8.1–213	8.9–323	6.3–230	8.9–323	6.3–230
Number of antennas <sup>a</sup>	34	33	36	33	36
Time on source	72 minutes	36 minutes	72 minutes	36 minutes	72 minutes
Flux calibrator	Callisto	Ganymede	Mars	Ganymede	Mars
Central $\nu$ (GHz)	114.195	87.830	87.823	88.390	88.382

**Note.**

<sup>a</sup> Omitting antennas flagged for most or all of the run.

$\sim 3''$  at  $\text{PA} = 215^\circ \pm 5^\circ$  (Elmegreen et al. 2000), nearly perpendicular to the major axis of the central star complex. The cone has an opening angle of  $\sim 60^\circ$ ; its darkest part is a column of width  $\sim 0''.5$ . The reddish region also contains the vertex of a V-shaped dust structure opening to the north. This vertex appears to coincide with the radio continuum peak and the Spitzer  $8\ \mu\text{m}$  emission peak. It may be the location of an embedded cluster old enough to host supernovae or some other source of nonthermal emission.

### 2.3. X-Rays: Possible ULX in the Core

In four *Chandra* observations between 2010 and 2013, Mineo et al. (2014) detect Feature i as an elongated soft X-ray source and suggest that it may contain a nonvariable ultra-luminous X-ray source (ULX) surrounded by hot diffuse gas. The possible ULX and the radio continuum peak coincide within the uncertainties.

### 2.4. Previous ALMA CO, HI, and SFR

The CO emission from Feature i has a C-shaped distribution and consists of two lobes that join in the core: one lobe along the opaque dust cone southwest of the central star complex and the other lobe along the extended  $8\ \mu\text{m}$  emission north-northwest of the core. The CO lobe along the dark dust cone has about the same length as the dark cone (Elmegreen et al. 2017), and thus the extinction of the dark cone is probably from dust associated with the cold molecular gas.

Because of the resolution of the HI data, Elmegreen et al. (2016) use a  $14''$  ( $=2.4\ \text{kpc}$ ) diameter aperture to measure the SFR, HI mass, and molecular mass of Feature i. They find the  $\text{SFR} = 1.6\ M_\odot\text{yr}^{-1}$  (from the combination of  $24\ \mu\text{m}$  and  $\text{H}\alpha$  luminosities), the HI mass  $M(\text{HI}) = 1.1 \times 10^8 M_\odot$ , and  $M(\text{H}_2) = 8.1 \times 10^7 M_\odot$  (multiply these values of the atomic and molecular mass by a factor of 1.36 to include helium). In this aperture, the HI velocity dispersion is high ( $52\ \text{km s}^{-1}$ ). The molecular gas consumption time in Feature i is only 50 Myr, and the total gas consumption time is 118 Myr. A somewhat smaller aperture,  $10''$  in diameter, captures essentially all of the ongoing star formation in Feature i (Smith et al. 2014), the extended radio and  $8\ \mu\text{m}$  emission, and the molecular mass (Elmegreen et al. 2017).

## 3. New Observations

### 3.1. CO, $\text{HCO}^+$ , HCN, and Millimeter-wave Continuum

Table 2 contains some observing details about our new ALMA  $^{12}\text{CO } J = 1 \rightarrow 0$ , HCN, and  $\text{HCO}^+$  observations of Feature i, Table 3 describes the resulting cubes and surface brightness

(integrated intensity) maps of the spectral lines, and Table 4 lists the properties of the line-free continuum maps associated with these observations. The notation  $\sigma_{\text{eff}}$  means the rms noise at Feature i after correction for primary-beam attenuation.

The ALMA  $^{12}\text{CO } J = 1 \rightarrow 0$  observations (rest  $\nu_0 = 115.271202\ \text{GHz}$ ) on 2015 May 15 were obtained during ALMA Cycle 2. They consist of mosaic maps made with 34 pointings, spaced  $26''$  apart, to cover the emission from the galaxy pair, with phase center at R.A., decl. (J2000) = 06 16 22.809,  $-21\ 22\ 30.73$ . The bandwidth is 1.875 GHz. The brightest millimeter-wave continuum source in the galaxy pair is Feature i, and it is well below the noise in the CO spectral-line cube. The maximum recoverable scale is  $15''$ , which exceeds the size of Feature i.

Using the pipeline with CASA 4.2.2 software, the ALMA Data Reduction Team did the calibration and flagging of the  $^{12}\text{CO } J = 1 \rightarrow 0$  observations and made and cleaned a data cube of the CO Cycle 2 line emission. Inspecting this, we saw no problems. For subsequent analysis, we used the AIPS software package. To select areas of genuine emission in the CO data, we convolved the cube before correction for primary-beam attenuation to  $3''$  resolution, clipped it at 2.5 times its rms noise, and retained regions of emission only if they appear in at least two adjacent velocity channels. The result was applied as a blanking mask to the original cube, and after correcting for primary-beam attenuation, we calculated the moment maps. Additionally, we blanked the intensity-weighted velocity field (first moment) and the velocity dispersion (second moment) images where the CO surface brightness is less than  $(2.5 \times \text{rms noise}) \times (2\ \text{channel widths})$ . Figure 3 displays the CO surface brightness (integrated intensity) map of Feature i from this cube.

We also combined our lower resolution ALMA Cycle 1 CO data (listed in Table 1) with our Cycle 2 CO data, then made and cleaned a data cube of the combined emission, and similarly masked it. The cube derived from the Cycle 2 data alone is called the CO Cycle 2 cube, and the one derived from the combined Cycle 1 plus Cycle 2 data is called the CO Combined cube. The CO Cycle 2 cube has the higher spatial resolution. The CO Combined cube has the higher velocity resolution and is more sensitive to extended emission. For the  $\sim 1''$  core and for where a clearer distinction between the core and the dark cone is needed, we use the CO Cycle 2 cube. For the velocity field in Section 7, we use the CO Combined Cube. Unless otherwise noted, our results are from the CO Cycle 2 cube, although for some applications, such as the extinction on a kiloparsec scale (Section 4.1), both CO cubes yield the same values.

On 2014 August 30 and 2015 June 7, we made ALMA observations of the spectral lines HCN ( $1-0$ ) (rest  $\nu_0 = 88.631601\ \text{GHz}$ ) and  $\text{HCO}^+$  ( $1-0$ ) (rest  $\nu_0 = 89.188526\ \text{GHz}$ )

**Table 3**  
New ALMA Spectral-line Cubes and Maps of Feature i

Parameter	CO Cycle 2	CO Combined	HCN	HCO <sup>+</sup>
Channel width	10 km s <sup>-1</sup>	4.87 km s <sup>-1</sup>	8 km s <sup>-1</sup>	10 km s <sup>-1</sup>
Weighting	Briggs $R = 0.5$	Briggs $R = 0.5$	Natural	Natural
PSF (HPBW)	1''.37 × 1''.04	1''.82 × 1''.33	1''.22 × 0''.95	1''.26 × 1''.00
PSF (BPA)	88°8	-73°4	-85°6	-81°7
Pixel size	0''.2	0''.2	0''.3	0''.3
$T_b/I^a$ (K/Jy beam <sup>-1</sup> )	65.6	38.6	137	124
At Feature i:				
$\sigma_{\text{eff}}$ per channel <sup>b</sup>	3.8	3.3	0.96	0.86
Peak S/N <sup>c</sup>	12	17	<2	3.7
Max. brightness <sup>d</sup>	1.45	2.44	...	0.062
$N(\text{H}_2)$ equivalent to 1 Jy beam <sup>-1</sup> km s <sup>-1</sup> in CO	189 $M_\odot$ pc <sup>-2</sup>	111 $M_\odot$ pc <sup>-2</sup>	...	...
Max. $N(\text{H}_2)$ in Feature i	281 $M_\odot$ pc <sup>-2</sup>	271 $M_\odot$ pc <sup>-2</sup>	...	...

**Notes.**

<sup>a</sup>  $T_b/I$  gives the brightness temperature  $T_b$  equivalent to a surface brightness  $I$  of 1 Jy beam<sup>-1</sup>.

<sup>b</sup>  $\sigma_{\text{eff}}$  (in mJy beam<sup>-1</sup>) is the rms noise at Feature i after correcting for primary-beam attenuation.

<sup>c</sup> Peak signal-to-noise ratio (S/N) in channel maps

<sup>d</sup> Maximum surface brightness (Jy beam<sup>-1</sup> km s<sup>-1</sup>) in the integrated intensity image of Feature i.

and also observations of the 100 GHz continuum. On 2014 August 30, the maximum recoverable scale is 11''–12''.5 for observations in the range 100–88 GHz; on 2015 June 7, it is 17''–20'' for these frequencies. Three fields in the galaxy pair were observed. The westernmost field has phase center R.A., decl. (J2000) = 06 16 17.654, -21 22 13.36, and includes Feature i near its western edge. Using the Pipeline-Cycle 2-R1-B and CASA 4.2.2 software, the ALMA Data Reduction Team did the calibration and flagging, combined the  $uv$  data from the two dates, and made and cleaned the continuum image and data cubes of the line emission.

In addition to the 100 GHz continuum map, we made a continuum map at 88 GHz from the line-free channels in the HCO<sup>+</sup> cube. In the HCO<sup>+</sup> channel maps, the maximum S/N is only  $3.7 \times \sigma_{\text{eff}}$ . To make a blanking mask for the HCO<sup>+</sup> cube, we followed the same procedure as with the CO data except that we convolved the HCO<sup>+</sup> cube to 2'' resolution rather than 3'' resolution and used a clip level of 2 times its rms noise. In the HCO<sup>+</sup> integrated intensity image at Feature i, a surface brightness  $I(\text{HCO}^+)$  of  $(2 \sigma_{\text{eff}}) \times (2 \text{ channel widths}) = 0.0344$  Jy beam<sup>-1</sup> km s<sup>-1</sup>, and the maximum value of the surface brightness  $I(\text{HCO}^+)$  is 0.062 Jy beam<sup>-1</sup> km s<sup>-1</sup>, displaced 0''.4 north, 0''.5 east of the radio continuum peak.

No HCN emission was detected in Feature i. This provides an upper limit on its HCN/CO ratio (see Section 6).

### 3.2. Near-IR K-band Spectra

On 2017 February 15, K-band spectra were taken of the core of Feature i with Gemini's NIFS integral field spectrograph under photometric conditions. NIFS is an image slicer integral field unit (IFU) with a field of view of 3'' and a pixel scale of 0''.1 × 0''.04. Due to the size of Feature i and the lack of suitable guide stars in the 3'' field, we observed in natural seeing mode. The resulting spatial resolution is estimated to be ~0''.5 or better. The precise R. A., decl. at field center is less well determined than if there were a guide star within the 3'' NIFS field.

Observations were done in a traditional ABBA pattern, to remove the sky contribution, repeated nine times with 150 s

exposures, where each exposure is an average of two coadds. The “A” position was centered on Feature i and the “B” position on a piece of blank sky identified in previous imaging.

The science data were reduced in a standard manner within the pyraf environment using the Gemini nifs package. Darks were subtracted and clean running sky frames constructed from the “B” frames. Wavelength calibration was performed using an argon/xenon lamp; the uncertainty in this calibration is less than 0.2 pixels in wavelength, equivalent to 12 km s<sup>-1</sup>. Because the spatial extent of the Br $\gamma$  emission determined by fitting a 2D Gaussian is 1''.1 (=190 pc; FWHM), we used a 1''.1 diameter aperture for extracting the spectrum of Feature i from the combined data cube.

A telluric star was observed before (HIP 23671) and after (HIP 34949) the science sequence in order to be able to correct for the absorption features in the spectra due to Earth's atmosphere. These were further used to flux calibrate the spectrum of Feature i, with a 1''.1 diameter aperture. Figure 4 presents the final corrected, calibrated, background-subtracted K-band spectrum of Feature i obtained with the 1''.1 diameter aperture. We identified redshifted Br $\gamma$ , H $_2$ , He I, and He II lines in the spectrum and performed a Gaussian fit to each line to measure its central wavelength, line width, and flux. The instrumental line width estimated from the width of the arc lines is  $1.6 \times 10^{-4}$   $\mu\text{m}$ , equivalent to 22 km s<sup>-1</sup> at Br $\gamma$ . This was then subtracted in quadrature from the line widths of the spectral lines detected in Feature i.

## 4. Extinction in Feature i

Table 5 lists estimates of  $A_v$  in various parts of Feature i. Except in the case of the “dark cone outside core,” these are  $A_v$  values to the midplane under the assumption that the gas and dust are symmetrically distributed about the midplane. Some details, discussion, and the molecular column densities are given below.

### 4.1. Extinction on Kiloparsec Scale

For the extinction in a 7''.2 (1.2 kpc) diameter aperture, which contains most of the CO emission from Feature i, all three types of

**Table 4**  
ALMA Continuum Maps of Feature i

Parameter	88 GHz <sup>a</sup>	100 GHz <sup>a</sup>	106.4 GHz <sup>b</sup>
Bandwidth	0.52 GHz	3.9 GHz	6 GHz
Weighting	Natural	Natural	Briggs R = 0.5
PSF (HPBW)	1".26 × 1".00	1".07 × 0".85	1".64 × 1".22
PSF (BPA)	-81.7°	-83.5°	-79.7°
Pixel size	0".1	0".1	0".2
$T_b/I$ (K/Jy beam <sup>-1</sup> )	125	134	54.3
$\sigma_{\text{eff}}$ (mJy beam <sup>-1</sup> )	0.068	0.034	0.044
Max. surface brightness <sup>d</sup>	1.33	0.79	1.04

**Notes.**

<sup>a</sup> Made along with HCN and HCO<sup>+</sup> observations on 2014 August 30 and 2015 June 7.

<sup>b</sup> Made along with CO Cycle 2 observations on 2015 May 15.

<sup>c</sup>  $\sigma_{\text{eff}}$  is the rms noise at Feature i after applying the correction factor for primary-beam attenuation.

<sup>d</sup> Units are mJy beam<sup>-1</sup>.

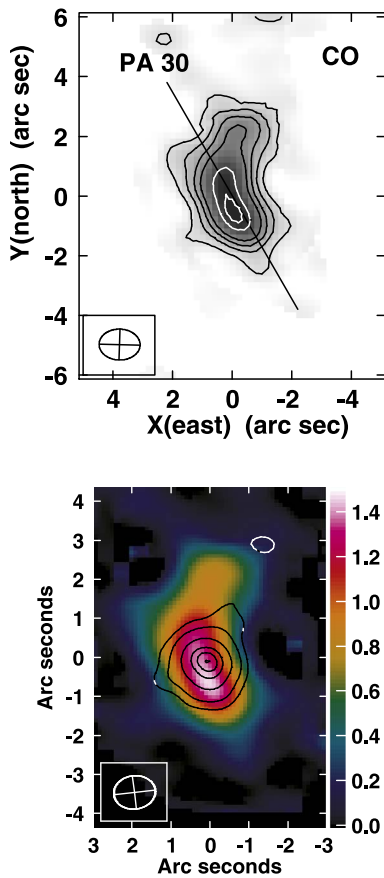


**Figure 3.** Top: grayscale and contour display of the CO surface brightness with contour levels at 0.2, 0.4, 0.6, 0.8, 1.2, and 1.4 Jy beam<sup>-1</sup> km s<sup>-1</sup>, where 1 Jy beam<sup>-1</sup> is equivalent to  $T_b = 65.6$  K, and 1 Jy beam<sup>-1</sup> km s<sup>-1</sup> corresponds to  $N(\text{H}_2) = 189 M_\odot \text{pc}^{-2}$ . The axis of the dark dust cone is represented by the line drawn at PA = 30°. Bottom: contours of the 100 GHz continuum emission overlaid on the color-coded CO image with contour levels at 3×, 6×, 12×, 18×, 21×, and 23× the rms noise  $\sigma_{\text{eff}}$  of 0.034 mJy beam<sup>-1</sup>, equivalent to  $T_b = 0.134$  K. The beam symbol represents the 100 GHz beam. The wedge is in units of Jy beam<sup>-1</sup> km s<sup>-1</sup>, with 1.0 units corresponding to  $N(\text{H}_2) = 189 M_\odot \text{pc}^{-2}$ . The radio and 100 GHz continuum peaks coincide, the maximum CO surface brightness is displaced 0".5 south of the radio peak, and the 100 GHz continuum emission is not elongated along the dark dust cone. Both panels are centered on the radio peak.

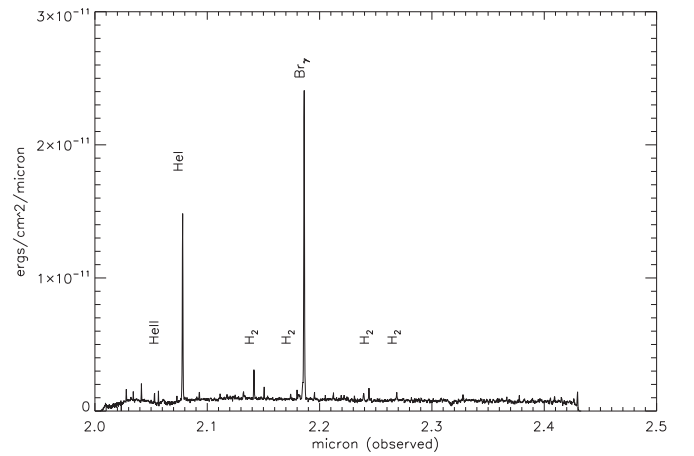


**Figure 4.** K-band spectrum of the core of Feature i from photometry with an aperture 1".1. The abscissa is the observed wavelength. Emission lines of Br $\gamma$ , He I, and He II, and the rovibrational lines of H $_2$  are marked.

methods in Table 5 are consistent with  $A_v = 3\text{--}3.5$  mag to the midplane. From the  $\text{H}\alpha/\lambda 6$  cm radio continuum ratio, the upper limit to  $A_v$  is obtained by taking the radio continuum emission as entirely thermal (which it is not), and the lower limit assumes the thermal fraction of the  $\lambda 20$  cm radio continuum emission is  $(10 \pm 3)\%$ . From the  $L(24 \mu\text{m})/L(\text{H}\alpha)$  ratio, Smith et al. (2014) find  $A_v$  equals 4 mag with a 10" diameter aperture. Adjusting to the 7".2 aperture gives 3.5 mag.

The mean line-of-sight column density  $N(\text{H}_2)$  of CO emission in the 7".2 aperture is  $(4.1 \pm 0.4) \times 10^{21}$  molecules cm<sup>-2</sup> ( $=66 \pm 7 M_\odot \text{pc}^{-2}$ ). Our HI observations, which did not resolve Feature i, have a mean atomic column density  $N(\text{HI}) = 3.4 \times 10^{21}$  atoms cm<sup>-2</sup> in the 13".5 × 12" HI HPBW. As we do not know about the clumping of HI within the HI synthesized beam, we adopt this mean value for  $N(\text{HI})$  here. With the standard Galactic relation between the neutral hydrogen column density and  $A_v$  (Bohlin et al. 1978), the resulting  $A_v$  from front to back is  $4.3 \pm 0.4$  mag from the molecular hydrogen and 1.8 mag from HI, for a total front-to-back  $A_v$  of 6.1 mag and thus  $\sim 3$  mag to the midplane if the gas and dust are symmetrically distributed about the midplane.

**Table 5**  
Mean Extinction in Various Parts of Feature i

Location	Indicator	$A_v^a$ (mag)	References
7''2 aperture <sup>b</sup>	H $\alpha$ / $\lambda$ 6 cm	<4.9	1
7''2 aperture <sup>b</sup>	H $\alpha$ / $\lambda$ 6 cm	$\geq 3.2 \pm 0.4$	2
7''2 aperture <sup>b</sup>	$L(24\mu\text{m})/L(\text{H}\alpha)$	3.5	3, 2
7''2 aperture <sup>b</sup>	$N(\text{H}_2)$	$2.2 \pm 0.2$	2
7''2 aperture <sup>b</sup>	$N(\text{H}_2) + N(\text{H I})$	$\sim 3$	2
Central star complex	HST <i>UBVI</i>	3.3	4
13 star complexes <sup>c</sup>	HST <i>UBVI</i>	$1.45 \pm 0.76$	4
Brightest H $\alpha$ emission <sup>d</sup>	H $\beta$ /H $\alpha$	0.74	5
1''6 aperture on core <sup>b</sup>	$N(\text{H}_2)$	7.5	2
At radio peak	$N(\text{H}_2)$	8.3	2
Dark cone outside core <sup>e</sup>	$N(\text{H}_2)$	4.7 <sup>f</sup>	2

#### Notes.

<sup>a</sup>  $A_v$  to midplane unless otherwise noted.

<sup>b</sup> Centered on radio peak.

<sup>c</sup> Mean of star complexes in cluster arcs outside of the core.

<sup>d</sup> 1'' diameter aperture centered on the brightest H $\alpha$  emission, which is 0''85 east, 2''3 south of radio peak, and thus outside of the core. The H $\alpha$  position uncertainty is  $\sim 1''$ .

<sup>e</sup> 1''6 diameter aperture centered at distance  $d = 2''$  from radio peak along PA = 217°.

<sup>f</sup>  $A_v$  is front to back for the dark cone outside core.

**References.** (1) Kaufman et al. (2012), (2) this paper, (3) Smith et al. (2014), (4) Elmegreen et al. (2017), (5) Rupke et al. (2010).

#### 4.2. Extinction in the Core and Dark Dust Cone

The gas column density gives a much higher value of the extinction in the core of Feature i than the value deduced from the *UBVI* magnitudes of the 0.6 Myr central star complex (see Table 5). With a 1''6 diameter aperture (to approximate the synthesized beam area of the CO Cycle 2 data) centered on the radio continuum peak, the mean value of  $N(\text{H}_2)$  is  $(1.41 \pm 0.04) \times 10^{22}$  molecules  $\text{cm}^{-2}$  ( $= 226 \pm 7 M_\odot \text{pc}^{-2}$ ), equivalent to a front-to-back  $A_v$  of 15 mag based on the molecular gas alone. It is dominated by the portion of the opaque dust cone in this aperture. The maximum CO surface brightness, located at the apex of the dark cone, is displaced  $0''5 \pm 0''17$  south of the radio continuum peak (see Figure 3). The molecular column density  $N(\text{H}_2)$  is  $1.75 \times 10^{22}$  molecules  $\text{cm}^{-2}$  at the CO surface brightness maximum and  $1.62 \times 10^{22}$  molecules  $\text{cm}^{-2}$  at the radio peak. The latter is equivalent to a front-to-back  $A_v$  of 16.5 mag based on the molecular gas alone plus a contribution (possibly 1.8 mag as in Section 4.1) from  $N(\text{H I})$ . If the gas at the radio peak were distributed symmetrically about the midplane, then  $A_v = 8.3$  mag to the midplane from dust associated with the molecular gas there. Although starbursts tend to have lower values of  $X_{\text{CO}}$  by a factor of  $\sim 4$ , with a large dispersion in the amount of reduction (Bolatto et al. 2013), the extinction required to account for the opaque dust cone implies that the value of  $X_{\text{CO}}$  on the dark cone (where the extinction is too high to be measured optically) is not appreciably reduced from the standard value.

Measuring  $N(\text{H}_2)$  farther out along the optically opaque dust cloud, specifically with a 1''6 diameter aperture centered at a distance  $d = 2''$  from the radio peak along PA = 217° gives  $N(\text{H}_2) = (4.4 \pm 0.4) \times 10^{21}$  molecules  $\text{cm}^{-2}$  ( $= 70 \pm 7 M_\odot \text{pc}^{-2}$ ), equivalent to a front-to-back extinction of 4.7 mag from molecular gas alone. If this gas were symmetrically distributed about the midplane, then  $A_v$  to the midplane would be 2.3 mag

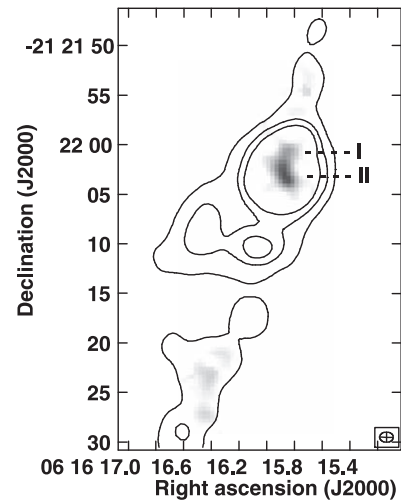


**Figure 5.** Location of the spiral arm near Feature i is outlined by contours of Spitzer 8  $\mu\text{m}$  emission at 4, 8, and 12  $\text{MJy sr}^{-1}$ . These are overlaid on  $I(\text{CO})$  in grayscale. The CO lobe of Feature i along the extended 8  $\mu\text{m}$  emission NNW of the core is labeled I, and the CO lobe along the dark dust cone is labeled II.

from molecular gas plus a contribution from H I. If we use the same value of  $N(\text{H I})$  as in Section 4.1, then  $A_v$  to the midplane =  $(2.3 + 0.9)$  mag = 3.2 mag, which is not sufficient to explain the dark dust cone which is optically thick even in the *I* band. The implication is that almost all of the gas in this part of the dark dust cone must be on the near side (relative to us) of the NGC 2207 disk.

#### 4.3. Comment about Extinction and X-Rays from Feature i

The possible ULX detected with *Chandra* lies at, or close to, the radio continuum peak and is slightly offset to the northwest of the 0.6 Myr central star complex. This star complex is too young to host a ULX. Neither Mineo et al. (2014) nor Smith et al. (2014) measure the X-ray extinction  $A_X$  within the Feature i core. Assuming an  $A_v$  of 4 mag to the midplane, Smith et al. (2014) deduce the value of  $A_X$  and get a dereddened  $L_X \sim 2 \times 10^{40}$  erg  $\text{s}^{-1}$  for the 0.5–10 keV luminosity of the central source in Feature i. Their value of  $L_X$  can be accommodated by a stellar-mass black hole with geometric beaming (Madau 1988) or inhomogeneous accretion (Ruszkowski & Begelman 2003). Because the extinction at the potential ULX is probably much higher than Smith et al. (2014) assumed (see Table 5 regarding  $A_v$  at the radio peak), the dereddened value of  $L_X$  may be considerably greater than this, and thus the possible ULX could be an intermediate-mass black hole.

### 5. The Two Lobes of CO Emission

In Figure 5, the location of the spiral arm near Feature i is outlined by a few contours of 8  $\mu\text{m}$  emission overlaid on CO in grayscale. CO lobe I, marked in this figure, lies along the major axis of the extended 8  $\mu\text{m}$  emission of Feature i north-northwest of the core at PA =  $-25^\circ$ , and thus is molecular gas in the disk of NGC 2207. In the core, it joins CO lobe II, which coincides with the opaque dust cone at a PA of  $210^\circ$ . As pointed out in Section 4.2, lobe II needs to be in front of the disk to account for the extinction of the dark cone.

According to encounter simulation models (Elmegreen et al. 1995a; Struck et al. 2005), the minor axis of the projection of the main disk of NGC 2207 into the sky plane is at PA =  $50^\circ$

$-70^\circ$ , with the near side (relative to us) in the northeast, and the central disk of NGC 2207 has an inclination  $i = 35^\circ \pm 5^\circ$  ( $i = 0^\circ$  for face on). The opaque dust cone extends toward the southwest of the core at  $PA = 215^\circ \pm 5^\circ$ , not far from the minor axis of this projection. Thus, unless the disk at Feature i is highly warped, gas flowing toward us from the center of the Feature i core in a direction quasi-perpendicular to the NGC 2207 disk would appear in projection to lie along the dark dust cone.

Figure 3 reveals that some of the CO emission with  $I(\text{CO}) \geq 1.2 \text{ Jy beam}^{-1} \text{ km s}^{-1}$  extends northeast of the radio peak for  $\sim 1''$  along a PA not far from that of the dust cone on the opposite side. Compared to the opaque cone, this bright northeast CO emission region has less extinction (see Figure 2) and thus less gas and dust in front of the midplane. Section 7 presents kinematical evidence that the dark cone is from gas approaching us on the near side of the midplane and some of the bright northeast CO emission may be from gas receding from us on the far side.

## 6. Core of Feature i and Left Fork of Red V

### 6.1. Overview of CO, 100 GHz Continuum, $\text{HCO}^+$ , and HCN

The resolution of the CO, 100 GHz continuum, and  $\text{HCO}^+$  images is about the same as the FWHM of the core (see Table 3 and Table 4). The bottom panel of Figure 3 displays contours of the 100 GHz continuum emission of Feature i overlaid on the CO surface brightness image. The 100 GHz continuum emission is not elongated along the dark dust cone. The locations of maximum surface brightness in the 100 GHz continuum, radio continuum, and Spitzer  $8 \mu\text{m}$  emission coincide within the uncertainties.

Figure 6, which overlays a few representative contours of  $\text{HCO}^+$ , CO, and 100 GHz emission in different colors on the HST color composite image of Feature i, reveals that the  $\text{HCO}^+$  emission lies roughly along the left fork of the red V in the HST image and diametrically opposite the CO emission from the dark dust cone. In the  $\text{HCO}^+$  image, emission at the  $0.035 \text{ Jy beam}^{-1} \text{ km s}^{-1}$  level extends along  $PA \sim 40^\circ$  from a radial distance  $r = 0''.3$  to  $r = 1''.3$  relative to the location of the radio continuum peak. The location and elongated shape of the  $\text{HCO}^+$  emission suggest that it may be produced by shock heating and excitation in a collimated wind from the energetic source at the radio peak (see the velocities in Section 7.1).

The critical density of  $\text{HCO}^+$  (1–0) is 100 times that of CO (1–0) (Juneau et al. 2009). Figure 6 (see Figure 3 for additional intermediate-level contours of CO and the 100 GHz continuum) indicates that the dense gas traced by  $\text{HCO}^+$  is more compactly distributed than the lower density molecular gas detected in CO or the 100 GHz continuum emission. The  $\text{HCO}^+$  image has a lower S/N than the CO or the 100 GHz continuum images. Also the CO distribution is somewhat smoother and more widespread than the  $\text{HCO}^+$  distribution, probably because the dense structures seen in  $\text{HCO}^+$  are only a small fraction compared to the CO-emitting gas;  $\text{HCO}^+$  may trace a few small clumps inside of larger molecular clouds.

The goal of HCN observations was to search for even denser molecular gas. No HCN emission is detected in Feature i. In particular, we do not detect HCN emission along the left fork of the red V where  $\text{HCO}^+$  is detected, even though both have about the same value of  $\sigma_{\text{eff}}$ . As an HCN upper limit for the core, we take  $I(\text{HCN}) = (2 \sigma_{\text{eff}}) \times (2 \text{ channel widths}) =$

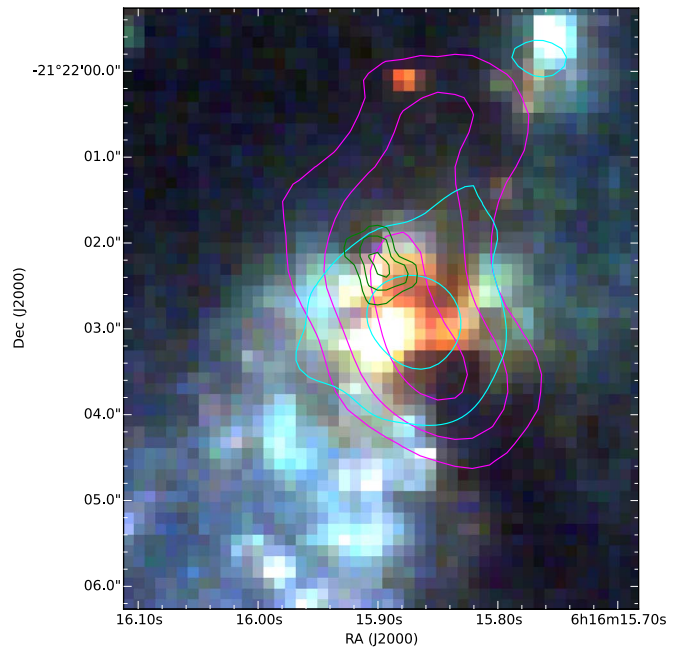


**Figure 6.** A few indicative surface brightness contours with CO in magenta, the 100 GHz continuum in cyan, and  $\text{HCO}^+$  in green overlaid on an HST color composite image of Feature i. This shows the correspondence between the dark dust cone and the southwest lobe of CO emission. Figure 3 displays additional intermediate-level contours of CO and the 100 GHz continuum. The contour levels of  $\text{HCO}^+$  are at 0.040, 0.050, and  $0.060 \text{ Jy beam}^{-1} \text{ km s}^{-1}$ , where  $1 \text{ Jy beam}^{-1}$  is equivalent to  $T_b = 124 \text{ K}$ , and  $(2 \sigma_{\text{eff}}) \times (2 \text{ channel widths}) = 0.0344 \text{ Jy beam}^{-1} \text{ km s}^{-1}$ . The  $\text{HCO}^+$  emission is diametrically opposite the CO emission from the dark cone and appears to lie roughly along the left fork of the red V-shaped dust structure opening to the north as seen in the HST image. The spatial resolutions are  $\sim 1''.2$  for the CO and  $\text{HCO}^+$  images, and  $\sim 1''.0$  for the 100 GHz continuum.

$4.2 \text{ K km s}^{-1}$ . For CO, we use the mean surface brightness  $I(\text{CO}) = 78.7 \text{ K km s}^{-1}$  in a  $1''.6$  diameter aperture centered on the radio peak, as this approximates the CO synthesized beam area. This gives an upper limit to the surface brightness ratio  $I(\text{HCN})/\text{mean } I(\text{CO})$  of 0.05. Using the same aperture for  $\text{HCO}^+$ , we obtain a mean  $I(\text{HCO}^+) = 3.4 \text{ K km s}^{-1}$  and thus the ratio  $I(\text{HCO}^+)/I(\text{CO}) = 0.044$  in the Feature i core. Some of the measured CO emission of the core is from molecular gas ejected quasi-perpendicularly to the stellar disk (see Section 7).

Feature i as a whole has a lower  $\text{H}_2/\text{HI}$  ratio than almost all of the positions in the studies by Usero et al. (2015) and Bigiel et al. (2016) of HCN-to-CO and FIR-to-HCN ratios at various locations in other disk galaxies. These authors note that clumps with a low  $\text{H}_2/\text{HI}$  ratio tend to have a lower HCN-to-CO ratio; the upper limit to HCN/CO in the Feature i core seems consistent with this trend. Comparable in SFR to the clump with the highest SFR in the overlap part of the Antennae galaxies, Feature i may be similar to it in terms of tracers of dense gas. For this Antenna clump (which contains SSC B1), Bigiel et al. (2015) measure a HCN-to-CO luminosity ratio of 0.027 (which is below our upper limit for the Feature i core), and, at the location of its HCN peak, an  $I(\text{HCO}^+)/I(\text{CO})$  ratio of 0.055 (25% higher than what we find in the Feature i core) and an  $I(\text{HCO}^+)/I(\text{HCN})$  ratio of 1.67.

In comparison, the M82 central starburst, because of its high  $I(\text{HCO}^+)/I(\text{HCN})$  ratio of 1.50 (Krips et al. 2008) and numerous SNe, is considered a late-stage starburst in which HCN is being depleted, either consumed in star formation or dissipated by turbulence or expelled via winds and feedback



**Table 6**  
Emission Lines in the *K*-band Spectrum of the Feature i Core<sup>a</sup>

Line	$\lambda_0$ ( $\mu\text{m}$ )	$\lambda_{\text{obs}}$ ( $\mu\text{m}$ )	$v_{\text{b,c}}$ ( $\text{km s}^{-1}$ )	$\sigma_v^{\text{b,d}}$ ( $\text{km s}^{-1}$ )	$F^{\text{b,e}}$
Br $\gamma$	2.16612	2.18625	$2786 \pm 1$	$35 \pm 1$	$19.7 \pm 0.1$
H <sub>2</sub> 1–0 S(2) <sup>f</sup>	2.03376	2.05302	$2839 \pm 3$	$12 \pm 3$	$0.42 \pm 0.02$
H <sub>2</sub> 1–0 S(1)	2.12183	2.14160	$2793 \pm 1$	$27 \pm 1$	$1.49 \pm 0.03$
H <sub>2</sub> 1–0 S(0)	2.22329	2.24394	$2784 \pm 3$	$25 \pm 3$	$0.77 \pm 0.02$
H <sub>2</sub> 2–1 S(2)	2.15421	2.17423	$2786 \pm 4$	$24 \pm 4$	$0.23 \pm 0.01$
H <sub>2</sub> 2–1 S(1)	2.24772	2.26867	$2794 \pm 4$	$39 \pm 4$	$0.51 \pm 0.02$
He I	2.05869	2.07807	$2822 \pm 1$	$33 \pm 1$	$10.2 \pm 0.1$
He II <sup>f</sup>	2.03788	2.05654	$2745 \pm 3$	unresolved	$0.36 \pm 0.02$

**Notes.**

<sup>a</sup> Measured with a  $1''.1$  diameter aperture.

<sup>b</sup> The listed uncertainties are from the rms noise and fitting the line profiles.

<sup>c</sup> The uncertainty from the wavelength calibration is  $\pm 12 \text{ km s}^{-1}$ .

<sup>d</sup> Velocity dispersion  $\sigma_v$  corrected for instrumental line width of  $22 \text{ km s}^{-1}$  at Br $\gamma$ .

<sup>e</sup> The flux  $F$  integrated over the line in units of  $10^{-15} \text{ erg s}^{-1} \text{ cm}^{-2}$ . It has not been corrected for extinction. Uncertainty from calibration and sky subtraction is about 10%.

<sup>f</sup> The centroid and  $\sigma_v$  of the H<sub>2</sub> 1–0 S(2) line may have been affected by the residuals from subtracting a neighboring night-sky line. The He II line is partly contaminated by a night-sky line.

(Baan et al. 2008; Krips et al. 2008; Kepley et al. 2014). In less dense gas, HCO<sup>+</sup> is more efficiently excited than HCN (Costagliola et al. 2011). Feature i may also be a late-stage starburst. For Feature i as a whole, Elmegreen et al. (2016) note that the molecular gas consumption time is 50 Myr.

### 6.2. The Core in Near-infrared Spectral Lines

The spatial resolution of the *K*-band observations is  $\sim 0''.5$  or better, so somewhat better than that of the radio and millimeter-wave images. The distributions of Br $\gamma$ , He I, and *K*-band continuum emission have an FWHM of  $1''.1$  (=190 pc), which exceeds the  $0''.6 \times 0''.4$  size of the 0.6 Myr central star complex. Table 6 lists the detected *K*-band emission lines and their properties measured with a  $1''.1$  diameter aperture. The H<sub>2</sub> rest wavelengths are from the wavenumbers in Black & van Dishoeck (1987). A single Gaussian extrapolation to a diameter of  $2''$  would increase the values of the flux  $F$  by a factor of 1.18, compared to those in this table. Although there is slightly more extended emission, this should be a reasonable approximation to the total flux. The listed values of the velocity dispersion  $\sigma_v$  have been corrected for instrumental line width. The Br $\gamma$  and He I lines have  $\sigma_v = 35 \pm 1 \text{ km s}^{-1}$ , and the H<sub>2</sub> 1  $\rightarrow$  0 S(1) line has  $\sigma_v = 27 \pm 1 \text{ km s}^{-1}$ . Thermal broadening at an electron temperature  $T_e$  would produce a  $\sigma_v$  of only  $12 \times (T_e/10^4\text{K})^{1/2} \text{ km s}^{-1}$ . Massive Oe stars and WN stars have line widths that are an order of magnitude greater than the measured Br $\gamma$  line width of Feature i, but winds from such stars could help power turbulence and expansion of the ionized gas in the core. As a comparison, the SSC B1 in the Antennae overlap region has Br $\gamma$  and H<sub>2</sub> 1  $\rightarrow$  0 S(1) velocity dispersions of  $45 \pm 4 \text{ km s}^{-1}$  and  $22 \pm 7 \text{ km s}^{-1}$ , respectively (Herrera & Boulanger 2017), for a region with a Br $\gamma$  FWHM size of 70 pc. Thus, the Br $\gamma$  velocity dispersion of the Feature i core is somewhat less than that for SSC B1 in the Antennae, but both have similar values of the H<sub>2</sub> 1  $\rightarrow$  0 S(1) line width.

Figure 7 presents in grayscale the Br $\gamma$  image rebinned to  $0''.05 \times 0''.05$  pixels with contours of Br $\gamma$ , H<sub>2</sub> 1  $\rightarrow$  0 S(1), and *K*-band continuum overlaid. The images have been smoothed with a 3 pixel smoothing kernel. From the Gaussian fits to the

surface brightness distribution, the location of maximum surface brightness in H<sub>2</sub> 1  $\rightarrow$  0 S(1) is displaced a minor amount,  $\sim 0''.15$ , northwest of the Br $\gamma$  peak, but aside from this, there is no strong difference between the spatial distributions of H<sub>2</sub> 1  $\rightarrow$  0 S(1), Br $\gamma$  emission, and *K*-band continuum.

We consider whether the ionized gas is bound to the central star complex. To estimate the escape velocity  $v_{\text{esc}}$ , we adopt from Mengel et al. (2002) the virial relation

$$v_{\text{esc}} = \left[ \frac{2GM_c}{\eta r_{\text{hp}}} \right]^{1/2}, \quad (1)$$

where  $r_{\text{hp}}$  is the projected half-light radius, the correction factor  $\eta = 6\text{--}10$  depends on the mass distribution, and  $M_c$  is the cluster mass. For the central star complex, we take  $r_{\text{hp}}$  as the geometric mean radius = 42 pc. The cluster mass  $M_c$  is the sum of the stellar mass,  $2 \times 10^6 M_\odot$ , plus the mass of ionized gas within the star complex. In Section 6.3 below, we assume a Gaussian distribution of electron density in the Feature i core and find the total mass of ionized gas in the core  $\simeq 1.7 \times 10^7 M_\odot$ . This is an upper limit to the mass of ionized gas within the star complex, so  $M_c < 1.9 \times 10^7 M_\odot$ , and thus  $v_{\text{esc}} < 62 \text{ km s}^{-1}/\eta^{1/2} = 20\text{--}25 \text{ km s}^{-1}$ , which is somewhat less than the observed Br $\gamma$   $\sigma_v$  of  $35 \text{ km s}^{-1}$ . We attribute the high velocity dispersion in the *K*-band spectral lines to a combination of high turbulence plus some expansion of the ionized gas. The shape of the Br $\gamma$  line profiles provides no evidence of a one-sided outflow. Figure 8 displays the Br $\gamma$  line profile, the Gaussian fit, and the residuals after subtracting the Gaussian fit at each position. The central panel is located at the Br $\gamma$  peak, and the panels are spaced  $0''.5$  apart. This provides an upper limit of  $22 \text{ km s}^{-1}$  (the instrumental line width) to a nonsymmetric outflow but does not rule out a spherical expansion of the ionized gas. Gaussian fits to the Br $\gamma$  line profile at each position in the field show no systematic change in centroid wavelength or in line width across the region, except that the line widths may be slightly broader at the outskirts of the region where the S/N is worse.

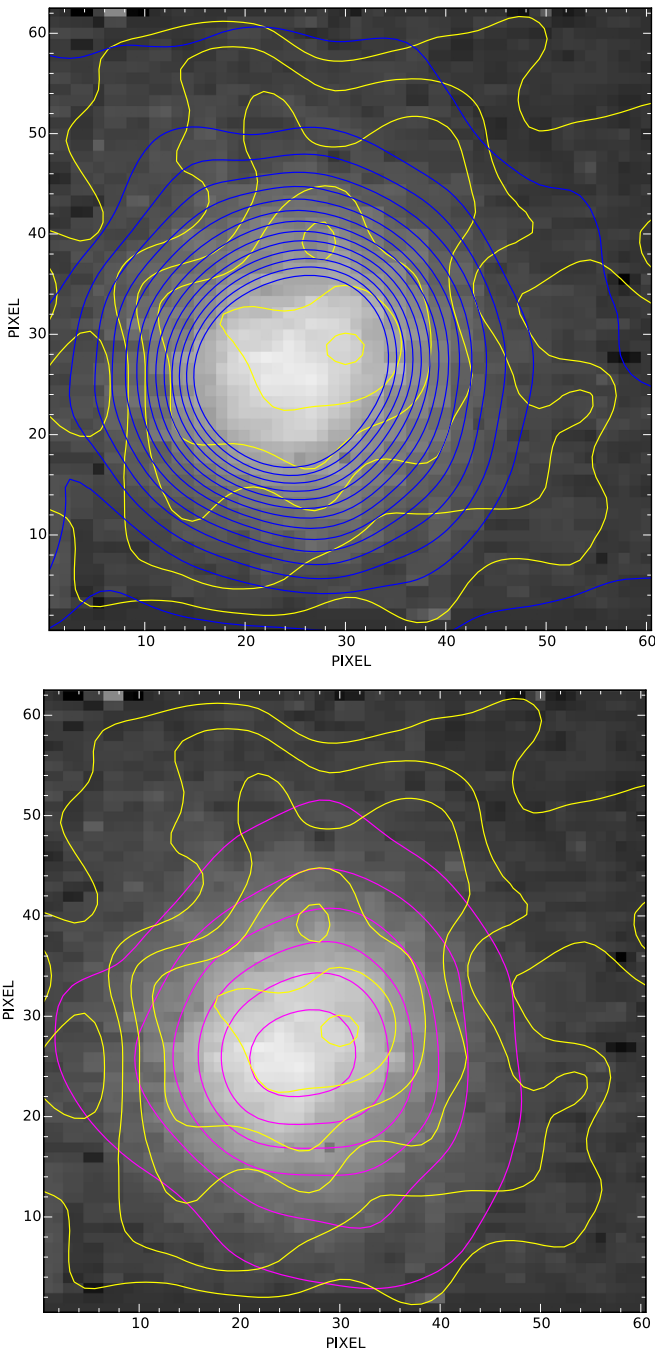


**Figure 7.** Surface brightness images of near-IR emission from the Feature i core. Top: contours of  $\text{Br}\gamma$  in blue and  $\text{H}_2 1 \rightarrow 0 \text{ S}(1)$  in yellow overlaid on  $\text{Br}\gamma$  in grayscale. Bottom: contours of  $K$ -band continuum in magenta and  $\text{H}_2 1 \rightarrow 0 \text{ S}(1)$  in yellow overlaid on  $\text{Br}\gamma$  in grayscale. The location of maximum surface brightness in  $\text{H}_2 1 \rightarrow 0 \text{ S}(1)$  is displaced a minor amount,  $\sim 0''.15$ , northwest of the  $\text{Br}\gamma$  peak, but aside from this, there is no strong difference between the spatial distributions of  $\text{H}_2 1 \rightarrow 0 \text{ S}(1)$ ,  $\text{Br}\gamma$  emission, and  $K$ -band continuum. In both panels, the lowest contour is  $3\times$  the rms noise measured in the corners of the image. The pixel size is  $0''.05 \times 0''.05$ , and the resolution is  $\sim 0''.5$  or better.

We compare the measured value of the flux  $F(\text{Br}\gamma) = (2.0 \pm 0.2) \times 10^{-14} \text{ erg s}^{-1} \text{ cm}^{-2}$ , uncorrected for extinction, with that expected from ionized gas associated with the 0.6 Myr central star complex. Models by Sternberg et al. (2003) predict a Lyman continuum rate  $N_{\text{Lyc}} = 2 \times 10^{53} \text{ s}^{-1}$  for an instantaneous burst of star formation with cluster mass  $2 \times 10^6 M_{\odot}$  at age 0.6 Myr, i. e., the values of mass and age of the

central complex that Elmegreen et al. (2017) find by adopting the same initial mass function (IMF; Salpeter with  $M_{\text{L}} = 1 M_{\odot}$ ,  $M_{\text{U}} = 120 M_{\odot}$ ) as in Sternberg et al. (2003).

For the 35 Mpc distance of NGC 2207, the expressions in Condon (1992) give

$$N_{\text{Lyc}} = 1.2 \times 10^{67} (T_e/10^4 \text{ K})^{0.31} F(\text{Br}\gamma), \quad (2)$$

where  $F(\text{Br}\gamma)$  in  $\text{erg s}^{-1} \text{ cm}^{-2}$  is extinction corrected, and no Lyman continuum photons are absorbed by dust or escape. With the above measured value of  $F(\text{Br}\gamma)$ , which is not corrected for extinction,  $N_{\text{Lyc}} = 2.4 \times 10^{53} \text{ s}^{-1}$  for  $T_e = 10^4$  or  $1.9 \times 10^{53} \text{ s}^{-1}$  for  $T_e = 5000 \text{ K}$ . Thus, most of the observed  $\text{Br}\gamma$  flux may result from Lyman continuum photons emitted by the 0.6 Myr central star cluster. With  $A_{\text{v}}$  equal to 3.3 mag for this star complex, then  $A_{\text{K}} = 0.112 A_{\text{v}}$  would be 0.37 mag (a factor of 1.4 in flux). In the optical HST images, the central star complex is the only star complex in the core, but there may be other ionization sources hidden behind the dark cone.

Generic models by Black & van Dishoeck (1987) of the excitation of  $\text{H}_2$  lines (see also the discussion by Rosenberg et al. 2013 and Doyon et al. 1994) predict the flux ratios 2–1  $\text{S}(1)/1\text{--}0 \text{ S}(1)$  and 1–0  $\text{S}(0)/1\text{--}0 \text{ S}(1)$  should have values  $\sim(0.53\text{--}0.56)$  and  $\sim 0.46$ , respectively, for excitation by UV radiation and  $\sim 0.1$  and  $\sim 0.2$  for excitation by collisions in shocks. For the  $\text{H}_2$  lines in the core of Feature i, the observed flux ratio of 2–1  $\text{S}(1)/1\text{--}0 \text{ S}(1)$  equals  $0.34 \pm 0.02$ , and the observed flux ratio of 1–0  $\text{S}(0)/1\text{--}0 \text{ S}(1)$  equals  $0.52 \pm 0.02$ . These values indicate that excitation by UV radiation rather than by collisions in shocks is probably dominant in the core. The similarity between the spatial distributions of  $\text{H}_2 1 \rightarrow 0 \text{ S}(1)$  and  $\text{Br}\gamma$  emission supports this interpretation.

The flux ratio of He I  $2.06 \mu\text{m}$  to  $\text{Br}\gamma$  is an indicator of the effective temperature  $T_{\text{eff}}$  of the stars producing the ionization, although the ratio is also sensitive to the electron density  $n_e$ , the dust content, and the geometry of the H II region (Doherty et al. 1995). In the Feature i core, this ratio has a value of 0.52, which is the maximum value in the model by Shields (1993) for  $n_e = 10^2 \text{ cm}^{-3}$ , and for that value of  $n_e$  implies  $T_{\text{eff}} = 4 \times 10^4 \text{ K}$  (Doherty et al. 1995). Although partly contaminated by a night-sky line, the presence of the He II  $2.04 \mu\text{m}$  line in the Feature i spectrum is indicative of high  $T_{\text{eff}}$ .

### 6.3. Radio and Millimeter-wave Continuum

Table 7 lists the results of two-dimensional Gaussian fits to the continuum emission from the Feature i core at various frequencies. For the 4.86 GHz radio continuum observations in 2001 and the Spitzer  $8 \mu\text{m}$  observations, both of which exhibit a bright core embedded in extended emission, the Gaussian fits employ the sum of two Gaussians plus a flat baseline, and only the Gaussian characterizing the core is listed here. For the rest of the data sets, the fit consists of a single Gaussian plus a flat baseline. The core of Feature i is the brightest source in NGC 2207/IC 2163 in the 100 GHz continuum, radio continuum, and  $8 \mu\text{m}$  emission, and all of the measurements in Table 7 get about the same value for its deconvolved FWHM,  $1''.0 \times 0''.7$  ( $170 \text{ pc} \times 120 \text{ pc}$ ). In the 100 GHz continuum, the core has a major axis PA of  $8^\circ \pm 10^\circ$ , which differs considerably from the  $-45^\circ$  major axis PA of the 0.6 Myr central star complex in the HST images.

After convolving the 88, 100, and 106 GHz continuum images to the same synthesized beam, we compare their flux

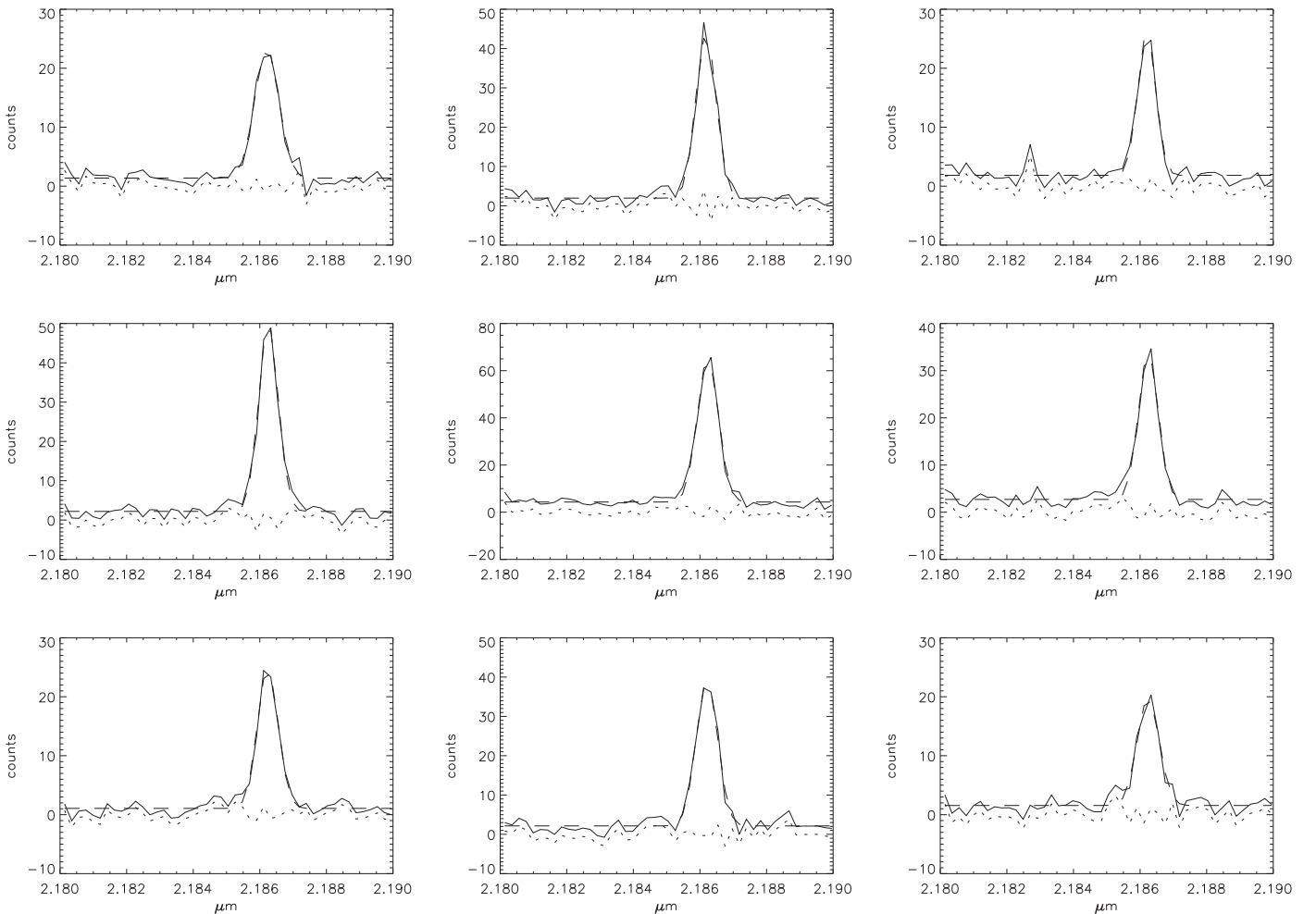


**Figure 8.** Br $\gamma$  line profiles and residuals after subtracting a single Gaussian plus a flat continuum fit at each position. The central panel is located at the Br $\gamma$  peak, and the panels are spaced  $0''.5$  apart. The solid curve is the observed profile, the dashed curve is the fit, and the dotted curve the residuals. The residuals provide no evidence of a one-sided outflow.

densities for the Feature i core and find an 88 to 106 GHz spectral index  $\alpha = -0.2 \pm 0.7$ . This rules out optically thin heated dust which would have  $\alpha = 3.8$  (Scoville et al. 2014) and free-free emission that is optically thick at 100 GHz (which would have  $\alpha = 2$ ) as major source(s) of the emission at 100 GHz. We infer that at 100 GHz, the main contributor to the flux density of the core is free-free emission that is optically thin at 100 GHz plus a contribution from nonthermal emission.

We need to reconcile the radio continuum and 100 GHz continuum flux densities of the Feature i core with the Br $\gamma$  flux. Based on the relations in Condon (1992) between optically thin free-free flux density  $S_{\text{ff}}$  and  $F(\text{Br}\gamma)$  for H II regions, we find that if  $T_e = 5000$  K, the measured value of  $F(\text{Br}\gamma)$  uncorrected for extinction corresponds to  $S_{\text{ff}}(100 \text{ GHz}) = 0.95 \pm 0.10$  mJy. Allowing for some extinction at Br $\gamma$ , this is the minimum to be consistent with  $F(\text{Br}\gamma)$ , and thus at least 67% of the 100 GHz flux density from the Feature i core needs to be optically thin free-free emission. We rule out  $T_e \geq 10^4$  K as otherwise the total  $S$  (100 GHz) of the core would be too small to account for the measured Br $\gamma$  flux.

In Table 7, the 1986 radio continuum observations by Vila et al. (1990) are a VLA scaled-array pair. Because for the core they measured  $S_{\nu}(4.86 \text{ GHz}) = 1.4$  mJy and a radio spectral index  $\alpha = -0.7$  (whereas optically thin free-free emission would have  $\alpha = -0.1$ ), the issue is how to get  $S_{\text{ff}}(100 \text{ GHz})$

$\sim 1$  mJy. We propose two types of ad hoc solutions: either (a) short-term variability of the nonthermal radio component with a decrease in the nonthermal component between 1986 March (when the 1.49 GHz emission was observed) and 1986 August (when the 4.86 GHz emission was observed), or (b) the presence of a component whose free-free emission is optically thick (and thus largely hidden) at 4.86 GHz but optically thin at 100 GHz. The actual explanation may be a combination of (a) and (b). In both cases, the nonthermal emission at 100 GHz may contain a contribution from nonthermal sources not detected at 4.86 GHz because of absorption.

Evidence for radio continuum variability of the core is the 1.26 mJy increase in its  $S_{\nu}(4.86 \text{ GHz})$  between 1986 and 2001. Although this may have been a radio supernova (Kaufman et al. 2012), it could have been some other type of energetic outburst. In Section 4.3, we argued that the possible ULX detected by Mineo et al. (2014) nearly coincident with the radio continuum peak could be an intermediate black hole because of the high extinction at that location. If so, it could serve as a source of short-term radio variability.

If variability of the nonthermal radio component in 1986 is the answer, we present the following example of how to satisfy  $S_{\text{ff}}(100 \text{ GHz}) \sim 1$  mJy. We assume that the free-free emission is optically thin for  $\nu \geq 1.49$  GHz. If  $S_{\text{ff}}(4.86 \text{ GHz})$  were 1.24 mJy, then  $S_{\text{ff}}(1.49 \text{ GHz})$  would be 1.40 mJy, and  $S_{\text{ff}}(100 \text{ GHz})$  would

**Table 7**  
Gaussian Fits to the Core of Feature i

Data	$S_\nu$ (mJy)	deconvolved size (FWHM, PA)	PSF (FWHM, BPA)
1.49 GHz <sup>a,b</sup>	3.4	$\sim 1''$	$1''.92 \times 1''.11, 9^\circ$
4.86 GHz <sup>a,c</sup>	1.4	$\sim 1''$	$1''.93 \times 1''.04, 169^\circ$
4.86 GHz <sup>d</sup>	$2.66 \pm 0.02$	$1''.20 \pm 0''.03 \times 0''.82 \pm 0''.03, 43^\circ \pm 4^\circ$	$2''.47 \times 1''.30, 8^\circ$
88 GHz	$1.50 \pm 0.16$	$0''.9 \pm 0''.2 \times 0''.8 \pm 0''.2, 155^\circ \pm 44^\circ$	$1''.26 \times 1''.00, -81.7^\circ$
100 GHz	$1.45 \pm 0.07$	$1''.03 \pm 0''.05 \times 0''.73 \pm 0''.06, 8^\circ \pm 10^\circ$	$1''.07 \times 0''.85, -83.5^\circ$
106.4 GHz	$1.52 \pm 0.12$	$1''.2 \pm 0''.2 \times 0''.6 \pm 0''.3, 167^\circ \pm 16^\circ$	$1''.64 \times 1''.22, -79.7^\circ$
$8 \mu\text{m}$	$14.3 \pm 0.02$	$1''.07 \pm 0''.03 \times 0''.70 \pm 0''.04, 17.5^\circ \pm 0.4^\circ$	$2''.4$

**Notes.**

<sup>a</sup> VLA scaled-array pair observations in 1986 by Vila et al. (1990).

<sup>b</sup> VLA radio continuum observations on 1986 March 18.

<sup>c</sup> VLA radio continuum observations on 1986 August 16.

<sup>d</sup> VLA radio continuum observations on 2001 April 14.

be 0.92 mJy, close to the minimum free-free flux density necessary if  $T_e \sim 5000$  K. Then, with an adopted spectral index  $\alpha_{\text{nth}} = -0.9$  for the nonthermal component, this would require the value of  $S_\nu(1.49 \text{ GHz})$  to have decreased from the observed 3.4 mJy in 1986 March to 1.9 mJy in 1986 August and the value of  $S_\nu(4.86 \text{ GHz})$  to have decreased from 2.1 mJy in 1986 March to the observed 1.4 mJy in 1986 August. Approximately the same changes in  $S_\nu(1.49 \text{ GHz})$  and  $S_\nu(4.86 \text{ GHz})$  between March and August would suffice to give  $S_{\text{ff}}(100 \text{ GHz}) = 0.92 \text{ mJy}$  if  $\alpha_{\text{nth}}$  were  $-0.7$ , or we could allow  $\alpha_{\text{nth}}$  to vary between the two dates.

Alternatively, if the nonthermal radio flux densities did not vary between 1986 March and 1986 August, we propose that some part of  $S_{\text{ff}}(100 \text{ GHz})$  arises from a component that is optically thick at 4.86 GHz but optically thin at 100 GHz. We extrapolate the flux densities from 4.86 to 100 GHz by assuming the measured  $S_\nu(100 \text{ GHz})$  of the core has the following components:

$$S_\nu = S_{\text{nth}} + S_{\text{ff,diffuse}} + S_{\text{ff,dense}}, \quad (3)$$

where  $S_{\text{nth}}$  is nonthermal emission,  $S_{\text{ff,diffuse}}$  is optically thin free-free emission at 4.86 GHz and at 100 GHz, and  $S_{\text{ff,dense}}$  is from an hypothesized group of ultradense H II regions (UD H II regions) that are optically thick at 4.86 GHz but optically thin at 100 GHz, with turnover frequency  $\nu_{\text{t,dense}}$  (at which  $\tau_{\text{ff,dense}} = 1$ ). Koblunicky & Johnson (1999) use the term UD H II region for the massive analog of an ultracompact H II region. The UD H II regions in Feature i would be analogous to the four UD H II regions in Henize 2–10 studied by Johnson & Koblunicky (2003).

Table 8 provides examples yielding  $S_{\text{ff}}(100 \text{ GHz}) = 1 \text{ mJy}$  for two different choices of  $S_{\text{ff,diffuse}}(4.86 \text{ GHz})$ , 0.7 mJy and 0.3 mJy [50% and 21%, respectively, of the observed  $S_\nu(4.86 \text{ GHz})$  in 1986] and two different choices of  $\nu_{\text{t,dense}}$ , 10 and 20 GHz. For free-free emission, the optical depth  $\tau_{\text{ff}} \propto \nu^{-2.1} a(\nu, T_e)$  (where the factor  $a(\nu, T_e)$  is  $\sim 1$  from Mezger & Henderson (1967)) and  $S_\nu \propto \nu^2 [1 - \exp(-\tau_{\text{ff}})]$ . This gives the values of  $\tau_{\text{ff,dense}}(4.86 \text{ GHz})$ ,  $S_{\text{ff,dense}}(4.86 \text{ GHz})$ , and the emission measure of the dense component  $\text{EM}_{\text{dense}}$  listed in Table 8. Subtracting the diffuse and dense components of the free-free emission from the total flux densities measured in 1986 produces the values of  $S_{\text{nth}}(4.86 \text{ GHz})$  and  $\alpha_{\text{nth}}$ . For the set of examples in Table 8, the nonthermal emission detected at

**Table 8**  
Examples Giving  $S_{\text{ff}}(100 \text{ GHz}) = 1 \text{ mJy}$  with  $T_e = 5000 \text{ K}$

Property	Values			
$S_{\text{ff,diffuse}}(4.86 \text{ GHz})$ (mJy)	0.70	0.70	0.30	0.30
$\nu_{\text{t,dense}}$ (GHz)	10	20	10	20
$S_{\text{ff,diffuse}}(100 \text{ GHz})$ (mJy)	0.52	0.52	0.22	0.22
$S_{\text{ff,dense}}(100 \text{ GHz})$ (mJy)	0.48	0.48	0.78	0.78
$\tau_{\text{ff,dense}}(4.86 \text{ GHz})$	4.64	20.5	4.64	20.5
$S_{\text{ff,dense}}(4.86 \text{ GHz})$ (mJy)	0.16	0.04	0.26	0.06
$\text{EM}_{\text{dense}}$ ( $10^8 \text{ pc cm}^{-6}$ )	1.6	6.9	1.6	6.9
$S_{\text{nth}}(4.86 \text{ GHz})^{\text{a}}$ (mJy)	0.54	0.66	0.84	1.04
$\alpha_{\text{nth}}$	-1.3	-1.2	-1.1	-0.91

**Note.**

<sup>a</sup> In 1986.

4.86 GHz in 1986 contributes, at most, 4.6% of the measured  $S_\nu(100 \text{ GHz})$ .

If the  $S_{\text{ff,dense}}(4.86 \text{ GHz})$  were from a single spherical UD H II region with uniform electron density  $n_e$ , then for the Table 8 examples, the UD H II region would have a radius of 5.3–2.0 pc and a proton column density  $N_p$  of  $(8\text{--}13) \times 10^{22} \text{ cm}^{-2}$ . Unless the dust-to-gas ratio is low within the UD H II region, the large values of  $N_p$  imply that the UD H II would have appreciable extinction in the K band. The free-free optical depth depends differently on density than the visual extinction does. Hence, a group of UD H II regions that are flattened along the line of sight with a nonuniform electron density and with the same values of  $\text{EM}_{\text{dense}}$  and  $\tau_{\text{ff,dense}}(4.86 \text{ GHz})$  as in Table 8 would have a lower K-band extinction than the single uniform sphere example.

To calculate the total mass of ionized gas in the core, we take  $S_{\text{ff}}(100 \text{ GHz}) \sim 1 \text{ mJy}$  for the core, assume a Gaussian distribution of electron density, and apply Equation A.14 of Mezger & Henderson (1967). The result is an H II mass of  $\sim 1.7 \times 10^7 M_\odot$  for the core.

We offer the following comment about warm dust emission at 100 GHz. Yang & Phillips (2007) obtain a median dust temperature  $T_d = 39 \pm 8 \text{ K}$  for 18 nearby LIRGs, and Wild et al. (1992) get  $T_d = 45 \text{ K}$  for the bulk of the ISM in the M82 starburst. Suppose warm dust contributes 7% (i. e., 0.1 mJy) of the measured  $S(100 \text{ GHz})$  of the Feature i core with  $T_d = 45 \text{ K}$  for the bulk of the ISM. Scaling Equation (12) of

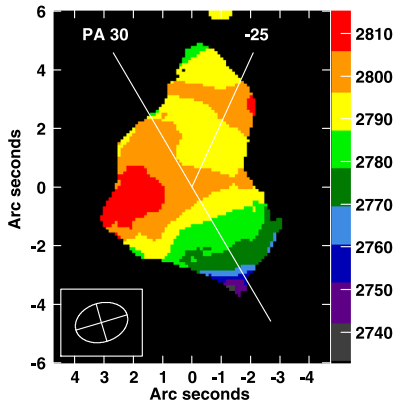


**Figure 9.** CO velocity field of Feature i from the CO combined data. The display is centered on the radio peak, and the axis of the dark dust cone is represented by the line drawn at PA = 30°. The extended 8  $\mu$ m emission from Feature i has its major axis at PA = -25°, which is also the PA of the CO lobe north-northwest of the core.

Scoville et al. (2014) to  $T_d = 45$  K then gives a core ISM mass  $M_{\text{ISM}}$  of  $7 \times 10^7 M_\odot$ . For the core, the CO flux density implies a molecular mass  $M(\text{H}_2)$  after including helium of  $3.4 \times 10^7 M_\odot$  with a  $2''.4$  diameter aperture (twice the geometric mean of the CO HPBW), and part of this molecular mass resides in the dark cone, so not in the disk. Therefore, an upper limit to the sum of the molecular plus H II mass of the core is  $\sim 5 \times 10^7 M_\odot$ . Either the contribution of warm dust emission to  $S(100 \text{ GHz})$  is less than 0.1 mJy or the H I mass of the core is at least comparable to its H II mass.

## 7. The Dark Dust Cone and Internal Kinematics of Feature i in Cold Gas

### 7.1. Measured Velocities

We consider whether there is kinematical evidence for the suggestion in Section 5 that the CO emission along the opaque dust cone is from gas outflowing perpendicular to the disk at Feature i. To get this gas in front of the midplane (relative to us), it needs to have a velocity component in our direction, and thus the CO emission from the dark cone should be blueshifted relative to the rest of Feature i.

Figure 9 displays the intensity-weighted velocity field (first-moment image) from the CO combined data. The channel width is  $4.87 \text{ km s}^{-1}$ ; this implies a velocity uncertainty of  $\pm 2.4 \text{ km s}^{-1}$ . Because Feature i is a two-lobed source in CO, the velocity field is complex. Figure 9 reveals that the velocity along the dark cone is blueshifted relative to the rest of Feature i. Using a  $1''.8$  diameter aperture (to approximate the synthesized beam area) centered along the dark cone (PA = 210°) at a distance of  $2''.0$  from the radio peak, we find the mean value of  $v$  is blueshifted by  $18 \text{ km s}^{-1}$  relative to its value at the radio peak.

Figure 10 displays  $^{12}\text{CO } J = 1 \rightarrow 0$  spectra of the core from the unmasked CO Cycle 2 data. The central panel is located at the radio continuum peak, the panels are spaced  $0''.4$  apart, and each individual line profile is an average over a  $0''.4 \times 0''.4$  box. Some of these line profiles exhibit an asymmetry or hint of more than one component. Thus, some of the velocity dispersion in the cold molecular gas may result from outflows or a blending of components rather than turbulence. From a Gaussian fit to the CO line profile at the radio peak, the FWHM line width corrected for the velocity resolution is  $42 \pm 1 \text{ km s}^{-1}$  (i.e.,  $(\sigma_v)_{\text{corr}} = 18 \pm 1 \text{ km s}^{-1}$ ). (With the unmasked CO combined data, the Gaussian fit

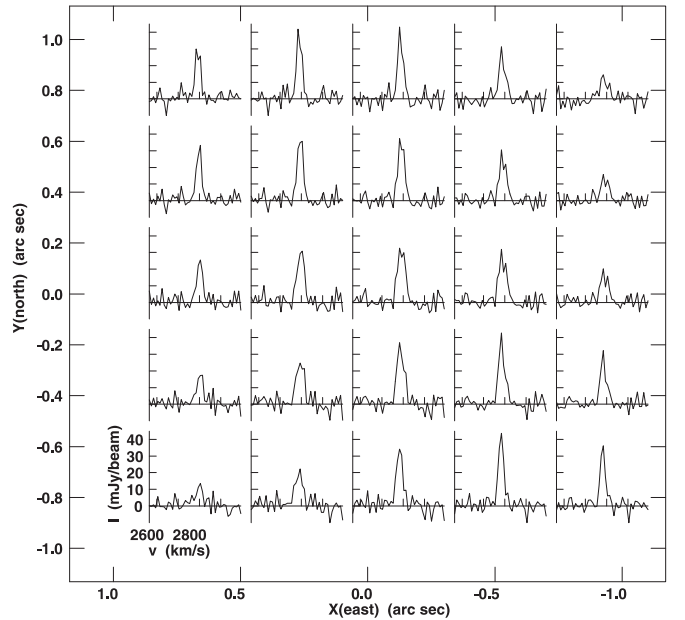


**Figure 10.** CO spectra of the core, spaced  $0''.4$  apart, from the CO Cycle 2 data. The central panel is at the radio continuum peak. The noise  $\sigma_{\text{eff}} = 3.8 \text{ mJy beam}^{-1}$ , equivalent to 0.25 K. Some of the line profiles are asymmetric, indicative of more than one component or outflow.

gives a slightly greater value of  $47 \pm 1 \text{ km s}^{-1}$  for the corrected FWHM line width.) In the velocity dispersion (second-moment) image, the velocity dispersion  $(\sigma_v)_{\text{corr}}$  at the radio peak is  $15 \text{ km s}^{-1}$ , and in the  $2'' \times 2''$  box displayed in this figure, the average  $(\sigma_v)_{\text{corr}} = 14 \pm 1 \text{ km s}^{-1}$ . Recall from Section 6.2 that Br $\gamma$  and the warm molecular gas traced by the infrared H $_2$  1  $\rightarrow$  0 S(1) lines have greater line widths than this with  $\sigma_v = 35 \text{ km s}^{-1}$  and  $27 \text{ km s}^{-1}$ , respectively, and that the spatial distribution of ionized and warm molecular gas is quite different from that of the cold molecular gas.

Figure 11 displays position–velocity diagrams: the top panel is from the CO Cycle 2 data and the bottom panel from the CO combined data. Both are centered on the radio peak and oriented along the dark cone at PA = 30°. On the abscissa, negative values of the plane-of-sky displacement  $d$  are on the dark cone; positive values of  $d$  are on the opposite side of the radio peak. The CO combined cube in the bottom panel reveals that the CO emission along the dark cone is present to  $d = -3''$ , consistent with the length of the visually opaque cone.

Because of its higher spatial resolution, the top panel of Figure 11 provides important detailed information, and the rest of our discussion here is based on it. Its two brightest emission knots are  $I(\text{CO}) = 46 \text{ mJy beam}^{-1}$  at  $d = -0''.8$  and  $I(\text{CO}) = 45 \text{ mJy beam}^{-1}$  at  $d = 1''.0$ . Each of these two molecular clumps bounding the ionized region in the core has a velocity of  $2784 \text{ km s}^{-1}$ , which we adopt as the disk velocity.

Most of the emission along the dark cone (negative values of  $d$ ) is blueshifted relative to this disk velocity. There are two outflow components to the CO emission from Feature i: (1) an approaching outflow component (labeled A in Figure 11) along the dark cone, and (2) a receding outflow component (labeled B) on the opposite side of the radio peak. Relative to the disk velocity, Component A is blueshifted by  $11 \text{ km s}^{-1}$  at the  $8\sigma_{\text{eff}}$  contour level and by  $16 \text{ km s}^{-1}$  at the  $6\sigma_{\text{eff}}$  contour level. For  $d = 0''$  to  $-2''$ , its outflow velocity appears roughly constant. Component B is redshifted by  $20 \text{ km s}^{-1}$  at the  $8\sigma_{\text{eff}}$  level and

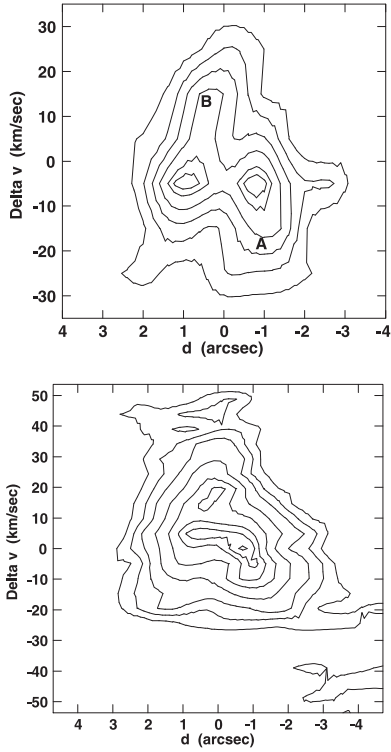


**Figure 11.** Position–velocity diagrams. In both panels, the center is at the location of the radio peak,  $\Delta v = 0$  corresponds to a velocity of  $2789 \text{ km s}^{-1}$ , and the abscissa is along  $\text{PA} = 30^\circ$ . Negative values of the displacement  $d$  are on the dark cone; positive values of  $d$  are on the opposite (northeast) side of the radio peak. Top: from the CO Cycle 2 cube with contours at  $2\times, 4\times, 6\times, 8\times, 10\times,$  and  $11\times \sigma_{\text{eff}}$ , where  $\sigma_{\text{eff}} = 3.8 \text{ mJy beam}^{-1} = 0.25 \text{ K}$ . Label A identifies an approaching outflow component on the dark cone, and Label B, a receding outflow component on the northeastern side of the radio peak. Bottom: from the CO combined cube with contours at  $2\times, 4\times, 6\times, 9\times, 12\times, 14\times, 15\times,$  and  $16\times \sigma_{\text{eff}}$ , where  $\sigma_{\text{eff}} = 3.3 \text{ mJy beam}^{-1} = 0.13 \text{ K}$ . More sensitive to extended emission, it reveals that CO emission from the dark cone is present to  $d = -3''$ .

by  $25 \text{ km s}^{-1}$  at the  $6\sigma_{\text{eff}}$  level relative to the disk velocity. Its outflow velocity decreases with distance from the center for  $d = 0''$  to  $1''.2$ . Because, compared to Component A, Component B does not extend as far and has a greater magnitude of outflow velocity, we infer it is from a more recent outburst than A. The difference in outflow velocities on the two sides of the radio peak explains why the intensity-weighted velocity at the radio peak is somewhat greater than the disk velocity based on the position–velocity diagram.

There is other evidence of outflowing cold molecular gas on the far side of the Feature i core. The detected  $\text{HCO}^+$  emission lies roughly along the left fork of the red V, i.e., on the opposite side of the radio peak from the dark dust cone. Restricting to positions where  $I(\text{HCO}^+)$  exceeds  $(2\sigma_{\text{eff}}) \times (2 \text{ channel widths})$ , we find that along the left fork of the red V from  $d = 0''.3$  to  $1''.3$ , the  $\text{HCO}^+$  velocity field has a redshift of  $8\text{--}16 \text{ km s}^{-1}$  relative to the CO disk velocity of  $2784 \text{ km s}^{-1}$ , and thus  $\text{HCO}^+$  is also participating in a redshifted outflow on the northeastern side of the radio peak.

The southwestern lobe of CO emission (CO lobe II in Figure 5) coincides with and has about the same length as the visually opaque dust cone. Attributing the blueshifted CO gas (Component A) along the dark cone to an outflow on the near side of the core is the only way to get enough cold molecular gas in front of the disk (relative to us) to explain the high  $A_v$  of

the opaque cone. For the redshifted gas (Component B) an outflow on the far side of the core is not the only possible interpretation as there could be noncircular motions in the disk (e.g., due to the spiral arm), but its location diametrically opposite the dark cone (see Figure 6) suggests that it is also an outflow.

Our HI data have too low a spatial resolution ( $13''.5 \times 12''$ ) for measuring outflows from the Feature i core. Instead, we compare HI velocities (Elmegreen et al. 1995b) and CO velocities (from the 2014 observations) averaged over a  $14''$  diameter aperture centered on the Feature i core: the mean velocity  $v \pm \text{rms}$  scatter is  $2769 \pm 11 \text{ km s}^{-1}$  in HI and  $2786 \pm 15 \text{ km s}^{-1}$  in CO. Feature i is located in the large area of NGC 2207 that has very broad and asymmetric HI line profiles. Averaged over the  $14''$  diameter aperture centered on Feature i,  $(\sigma_v)_{\text{corr}}$ , the velocity dispersion corrected for the velocity gradient across the HPBW is  $52 \pm 4 \text{ km s}^{-1}$  in HI and  $13 \pm 8 \text{ km s}^{-1}$  in CO.

## 7.2. Source of Outflows

We consider what powered the outflow of cold molecular gas to create the optically opaque dust cone extending  $3''$  from the center of the core. On the assumption that supernovae and stellar winds from O and WR stars integrated over their lifetimes supply the necessary mechanical energy, we estimate the SFR in the core required to produce the observed line-of-sight outflow velocities of the swept-up mass in the dark cone. The  $0.6 \text{ Myr}$  central star complex produces ionization and contributes to expansion of the H II region but is too young to provide most of the mechanical energy of the outflow or to account for the observed variable radio emission or the length of the dark cone. Because it is too young to have hosted a supernova, it is not a source of the cosmic-ray electrons necessary for the observed nonthermal radio emission. The  $0.6 \text{ Myr}$  star complex is the only star complex in the core detected in B-band, but older star complexes (up to  $60 \text{ Myr}$ ) are found elsewhere in Feature i. We conjecture that in the core there were previous generations of star formation whose optical emission is now hidden behind the high extinction near the radio continuum peak.

We assume the dark cone is perpendicular to the Feature i disk and adopt the following notation:  $i_{\text{feati}}$  is the inclination of the disk at Feature i,  $H_z = d / \sin i_{\text{feati}}$  is the perpendicular height of the dark cone above this disk,  $v_{\text{outflow}}$  is the observed line-of-sight component of the outflow velocity, and  $v_z = v_{\text{outflow}} / \cos i_{\text{feati}}$  is the component of the outflow velocity perpendicular to this disk. For the calculations below of the required mechanical energy, we adopt as representative values  $v_{\text{outflow}} = -13 \text{ km s}^{-1}$  on the dark cone and  $+23 \text{ km s}^{-1}$  on the opposite side of the radio peak.

## 7.3. Required Mechanical Energy and SFR

Simulations by Ceverino et al. (2012) of clumps with masses  $10^8\text{--}10^9 M_\odot$  in disk galaxies find that because angular momentum is approximately conserved during the clump's contraction, the spin vector of such a massive clump is generally aligned with the angular momentum vector of the disk in the clump's neighborhood. Because the total mass in gas of Feature i lies in this range, their results should apply to Feature i. If we ignore a possible warp of the NGC 2207 disk at Feature i and take  $i_{\text{feati}} = i$  of the central disk of NGC

$2207 = 35^\circ$ , then  $v_z = -16 \text{ km s}^{-1}$  on the dark cone and  $28 \text{ km s}^{-1}$  on the opposite side. These are low-velocity outflows, but the outflow velocities would have decreased as the molecular gas traveled away from the sources because of (a) the local potential well of the Feature i core, and (b) mass loading as the outflowing gas entrains surrounding gas;  $E_{\text{kin}}$  of bulk motion  $\sim M^{-1}$ , where  $M$  is the swept-up mass.

To estimate the mass of the outflowing molecular gas in the dark cone, we restrict our measurement to emission with velocities  $\leq 2774 \text{ km s}^{-1}$  in the CO Cycle 2 cube and sum the emission in the quadrant southwest of the radio peak. After correcting for helium, this gives  $M(\text{H}_2) = 8 \times 10^6 M_\odot$ . Of this mass, 36% lies on the dark cone at  $|d| \geq 1''.4$  from the radio peak, 25% at  $|d| \geq 2''.0$ , and only 4% at  $|d| \geq 2''.8$ . With  $M(\text{H}_2) = 8 \times 10^6 M_\odot$  and  $v_z = 16 \text{ km s}^{-1}$ , the estimated kinetic energy of bulk motion  $E_{\text{kin}} = 2 \times 10^{52} \text{ erg}$  for the dark cone. For the redshifted outflow on the far side of the core, the value of  $v_z^2$  is higher by a factor 3, but it is less extensive and its mass is unknown. On the assumption that the  $E_{\text{kin}}$  of the redshifted outflowing gas on the far side is comparable to that of the dark cone, the cumulative effect of supernovae and stellar winds in the core needs to produce a total  $E_{\text{kin}}$  of roughly  $4 \times 10^{52} \text{ erg}$  to power both outflows. Because, according to Castor et al. (1975), the amount of mechanical energy injected into the ISM by stellar winds from a single high-mass star integrated over its lifetime is comparable to that from a core-collapse supernova, we attribute half of this  $E_{\text{kin}}$  to supernovae.

We consider whether the SFR in the core of Feature i can achieve the required value of  $E_{\text{kin}}$ . Only about 0.1% of the energy of a supernova remains as  $E_{\text{kin}}$  of the bulk motions by the time the material has reached a few tens of parsecs from the explosion (Martizzi et al. 2015); see also Iffrig & Hennebelle (2017). Therefore, to get an  $E_{\text{kin}}$  of roughly  $2 \times 10^{52} \text{ erg}$  in this kind of wind from supernovae requires at least  $2 \times 10^4$  supernovae. Because it is hard to gather energy over more than 5–10 Myr because of the lifetimes of the progenitor stars of core-collapse supernovae and the crossing times, we need to have at least  $2 \times 10^4$  SNe occur in a time interval less than 10 Myr, if both the blueshifted and the redshifted outflows originated within the same 10 Myr period. A standard IMF gives about one supernova for every  $100 M_\odot$  of stars formed, so we would need an SFR  $> 0.2 M_\odot \text{ yr}^{-1}$  over 10 Myr to account for both outflows (or  $0.1 M_\odot \text{ yr}^{-1}$  to account for just the dark cone). Using a  $10''$  diameter aperture, Smith et al. (2014) find that the SFR of Feature i is  $1.7 M_\odot \text{ yr}^{-1}$  from the  $\text{H}\alpha$  and  $24 \mu\text{m}$  luminosities (sensitive to the SFR over the past 10 Myr) and  $1.5 M_\odot \text{ yr}^{-1}$  from  $24 \mu\text{m}$  and Galaxy Evolution Explorer NUV (sensitive to the SFR over a longer timescale). The distributions of millimeter-wave continuum, radio continuum, and  $8 \mu\text{m}$  emission imply that a significant fraction of this SFR occurs in the core, e.g., the core contributes 40% of the  $8 \mu\text{m}$  flux. Thus, it should be possible to satisfy the energy constraints with star formation at the current rate over 10 Myr.

We have not ruled out the possibility that nonthermal sources other than supernovae may also contribute to the mechanical energy.

For the CO outflow associated with the dark cone, CO emission is detected to a perpendicular height  $H_z \sim 0.9 \text{ kpc}$  above the disk, and the molecular mass  $M(\text{H}_2)$  at  $H_z > 600 \text{ pc}$  is  $\sim 2 \times 10^6 M_\odot$ . For this outflow  $H_z$  at  $d = -2''$  is  $590 \text{ pc}$ , and the time required for the molecular gas to travel from  $d = -1''$

to  $d = -2''$  with a constant speed  $v_z$  of  $16 \text{ km s}^{-1}$  would be 18 Myr.

In the encounter model by Elmegreen et al. (1995a), which reproduces the observed S-shape of the isovelocity contours in NGC 2207, the tidal force exerted by IC 2163 causes a warp of the outer disk of NGC 2207 with the northwestern part of NGC 2207 bent more toward us. If at Feature i the disk is warped with  $i_{\text{feati}} > i$  of the NGC 2207 central disk, then  $v_z$  and the required  $E_{\text{kin}}$  would be greater than in the unwarped disk case. If, averaged over 10 Myr, the SFR in the core powering just the dark cone outflow were  $0.2 M_\odot \text{ yr}^{-1}$  instead of the,  $0.1 M_\odot \text{ yr}^{-1}$  used above, then with the same arguments as above,  $v_z$  would be  $23 \text{ km s}^{-1}$  on the dark cone. With  $v_{\text{outflow}} = 13 \text{ km s}^{-1}$ , this gives  $i_{\text{feati}} = 55^\circ$ , and, assuming the warp has the same tilt axis as the central disk of NGC 2207, a galaxy warp at Feature i of  $55^\circ - 35^\circ = 20^\circ$ . Then, for the dark cone,  $H_z$  at  $d = -2''$  would be  $400 \text{ pc}$  and the time required for the molecular gas to travel from  $d = -1''$  to  $d = -2''$  with a constant speed  $v_z$  of  $23 \text{ km s}^{-1}$  would decrease to 9 Myr.

## 8. Possible Origin of Feature i

Because Feature i is an unusually active region, the question is how did it originate. The models by Struck et al. (2005) for the encounter between NGC 2207 and IC 2163 did not produce the spiral arms of NGC 2207. As discussed in some detail in that paper, this is because the encounter is retrograde with respect to NGC 2207, and thus the cumulative tidal forces on NGC 2207 are relatively weak. These models find that preexisting spiral arms in NGC 2207 are not destroyed by the interaction, but there are two strong effects that can impact the arms.

In the primary model of Struck et al. (2005), IC 2163 approaches NGC 2207 on the western side and swings  $180^\circ$  around the outer edge of the NGC 2207 disk to its present position on the eastern side. As pointed out by Struck et al. (2005), a significant amount of mass is pulled off IC 2163 and captured onto the disk of NGC 2207. However, most of this mass transfer occurs in a short time interval about halfway through the encounter and falls onto a different part of the disk from where Feature i is subsequently located. By the time the future Feature i passes closest to the transfer stream, the amount of mass transferred is much smaller, so it seems unlikely to trigger the most active region in the disk.

Struck et al. (2005) did not mention a second effect, which arises from the fact that IC 2163 pulls the nearest parts of the NGC 2207 disk backwards, against the orbital flow. The loss of angular momentum compresses the disk. Elmegreen et al. (1995b) find that, aside from the spiral arms, the radial brightness profile in  $B$  and  $R$  on the western side of NGC 2207 is relatively flat for radial distances  $40''$ – $90''$ , corresponding to the  $8 \text{ kpc}$ -wide HI ring and drops off steeply beyond  $90''$  (i.e., a little beyond Feature i). This unusually flat radial profile with a sharp cutoff is evidence of the compression of the disk resulting from loss of angular momentum. The compression and associated velocity gradients can produce or enhance clumpiness. In NGC 2207, five of the six very massive HI clouds, each with HI mass in excess of  $10^8 M_\odot$ , lie on the western or eastern portions of the HI ring/partial ring (see Figure 1). Although these massive HI clumps are likely to result, in part, from the bead instability of rings, the radial gradient in the angular momentum loss may have played a role in increasing their mass, either directly or by increasing the HI velocity

dispersion and thus the gravitational Jeans mass. Feature i lies on the spiral arm somewhat beyond the massive H I clouds N2 and N3 (see Figure 1). We speculate that at the location where Feature i subsequently developed, there was a large H I clump on the preexisting spiral arm, and the radial gradient in angular momentum loss created an inward crashing gas stream from the outer disk that hit the spiral arm at this clump as the disk of NGC 2207 rotated clockwise. The two intersecting flows enhanced the mass and density of the clump and triggered the starburst that became Feature i.

## 9. Conclusions

New ALMA  $^{12}\text{CO } J=1 \rightarrow 0$ ,  $\text{HCO}^+$ , and 100 GHz continuum observations and Gemini NIFS K-band spectra are presented and combined with previous HST optical, radio continuum, Spitzer, and H I data to study Feature i, a starburst clump on an outer arm of the interacting galaxy NGC 2207. Feature i has one of the highest SFRs among the set of 1700 star-forming complexes in interacting galaxies or normal spirals measured by Smith et al. (2016). In its grazing collision with IC 2163, NGC 2207 suffered a retrograde encounter, which caused the loss of angular momentum and compression of its outer disk. The double compression from the inward-flowing gas intersecting with an H I clump on the preexisting spiral arm may have produced Feature i.

One of the two CO emission lobes in Feature i coincides with an optically opaque dust cone extending a plane-of-sky distance  $\sim 500$  pc from the center of its 170 pc core. Our H I data have too low a spatial resolution for identifying this structure in H I. The CO column density can account for the dark cone extinction beyond the core only if almost all the gas and dust along the cone is on the near side (relative to us) of the NGC 2207 disk. In CO, we find two outflows of cold molecular gas, which we assume is streaming perpendicular to the galaxy disk: (a) along the dark cone an approaching outflow (consistent with the extinction argument) with velocity perpendicular to the disk  $v_z \sim 16 \text{ km s}^{-1}$  and an estimated molecular mass  $8 \times 10^6 M_\odot$ , and (b) on the opposite side, a receding outflow (also detected in  $\text{HCO}^+$ ) at  $v_z \sim 28 \text{ km s}^{-1}$ , but less extensive and of unknown mass. For the dark cone, the kinetic energy of bulk motion,  $\sim 2 \times 10^{52}$  erg, can be supplied by supernovae and the stellar winds of high-mass stars in the core if star formation at the observed rate is integrated over 10 Myr. If the NGC 2207 disk is not warped at Feature i, then the outflow along the dark cone is detected in CO to a height of  $\sim 0.9$  kpc above the disk.

The core contains a  $2 \times 10^6 M_\odot$  star complex with an age of 0.6 Myr. The measured  $\text{Br}\gamma$  flux of the core is consistent with that expected from this complex without requiring a top-heavy or otherwise unusual IMF. The  $\text{Br}\gamma$  and rovibrational  $\text{H}_2$  lines have FWHM line widths of  $82 \text{ km s}^{-1}$  and  $64 \text{ km s}^{-1}$ , respectively, probably a combination of high turbulence plus some expansion of the ionized gas. The symmetry of the  $\text{Br}\gamma$  line profile provides an upper limit of  $22 \text{ km s}^{-1}$  (the instrumental line width) to any (asymmetric) outflow of ionized gas.

In 2001, the  $\lambda 6$  cm radio continuum flux density of the core was nearly double that in 1986, indicative of either a radio supernova or some other type of energetic outburst. The possible ULX detected by Mineo et al. (2014) is nearly coincident with the radio continuum peak. Because of the very high extinction at that location, the measured X-ray flux of the

ULX could be consistent with an intermediate-mass black hole. Short-term radio variability associated with an intermediate-mass black hole would make it easier to reconcile the measured  $\text{Br}\gamma$  flux with the  $\lambda 6$  cm radio continuum flux density measured in 1986.

Our new observations combined with our own multispectral data set and data from the literature reveal Feature i to be a heavily obscured region of intense activity on an outer spiral arm. Given the  $\sim 2 \times 10^8 M_\odot$  mass of cold gas in Feature i, its precursor may have been analogous to the massive ( $10^8$ – $10^9 M_\odot$ ) H I clouds found in regions of high H I velocity dispersion in NGC 2207/IC 2163 and other galaxies undergoing close encounters (Kaufman et al. 1999). Some of the usual sites of highly luminous extranuclear star-forming clumps in large galaxies are (a) the overlap regions in galaxy mergers, e.g., the Antennae (Gilbert & Grapham 2007), (b) the hinge clumps produced by the multiple converging flows near the base of a tidal tail in prograde encounters, e.g., Arp 240 (Smith et al. 2014), and (c) the expanding ring of a collisional ring galaxy, e.g., the Cartwheel galaxy (Higdon 1995). Feature i illustrates that galaxies suffering close retrograde encounters in which loss of angular momentum by the outer disk causes disk contraction can also trigger the formation of a highly luminous star-forming clump under suitable conditions, e.g., if the gradient in angular momentum loss by the outer disk creates an inward crashing stream that collides with a massive H I cloud as it is being compressed by a spiral density wave.

This paper makes use of the following ALMA data: ADS/JAO.ALMA#2012.1.00357.S and ADS/JAO.ALMA#2013.1.00041.S. ALMA is a partnership of ESO (representing its member states), NSF (USA) and NINS (Japan), together with NRC (Canada), MOST and ASIAA (Taiwan), and KASI (Republic of Korea), in cooperation with the Republic of Chile. The Joint ALMA Observatory is operated by ESO, AUI/NRAO, and NAOJ. The National Radio Astronomy Observatory is a facility of the National Science Foundation operated under cooperative agreement by Associated Universities, Inc.

This paper presents observations obtained at the Gemini Observatory under program GN-2016B-FT-26. The Gemini Observatory is operated by the Association of Universities for Research in Astronomy, Inc. under a cooperative agreement with the NSF on behalf of the Gemini partnership: the National Science Foundation (United States), National Research Council (Canada), CONICYT (Chile), Ministerio de Ciencia, Tecnología e Innovación Productiva (Argentina), Ministério da Ciência, Tecnologia e Inovação (Brazil), and Korea Astronomy and Space Science Institute (Republic of Korea).








This research made use of the NASA/IPAC Extragalactic Database (NED), which is operated by the Jet Propulsion Laboratory, California Institute of Technology, under contract with the National Aeronautics and Space Administration.

We are grateful to Kartik Sheth for his generous help on this project and to Stephanie Juneau for early discussions about this research. We thank Jonathan Westcott for his contribution in obtaining the recalibrated ALMA  $uv$  data for Cycles 1 and 2 and the ALMA staff for doing the recalibration. We thank the referee for making detailed suggestions to improve the presentation of our results.

E.B. acknowledges support from the UK Science and Technology Facilities Council (grant number ST/M001008/1).



## ORCID iDs

Michele Kaufman  <https://orcid.org/0000-0002-5357-680X>  
 Bruce G. Elmegreen  <https://orcid.org/0000-0002-1723-6330>  
 Morten Andersen  <https://orcid.org/0000-0002-5306-4089>  
 Debra Meloy Elmegreen  <https://orcid.org/0000-0002-1392-3520>  
 Curtis Struck  <https://orcid.org/0000-0002-6490-2156>  
 Frédéric Bournaud  <https://orcid.org/0000-0002-5743-0250>  
 Elias Brinks  <https://orcid.org/0000-0002-7758-9699>

## References

- Baan, W. A., Henkel, C., Loenen, A. F., Baudry, A., & Wiklind, T. 2008, *A&A*, 477, 747
- Bigiel, F., Leroy, A. K., Blitz, L., et al. 2015, *ApJ*, 815, 103
- Bigiel, F., Leroy, A. K., Jimenez-Donaire, M. J., et al. 2016, *ApJL*, 822, L26
- Bigiel, F., Leroy, A. K., Walter, F., et al. 2008, *AJ*, 136, 2846
- Black, J. H., & van Dishoeck, E. F. 1987, *ApJ*, 322, 412
- Bohlin, R., Savage, B., & Drake, J. 1978, *ApJ*, 224, 132
- Bolatto, A. D., Wolfire, M., & Leroy, A. K. 2013, *ARA&A*, 51, 207
- Castor, J., McCray, R., & Weaver, R. 1975, *ApJL*, 200, L107
- Ceverino, D., Dekel, A., Mandelker, N., et al. 2012, *MNRAS*, 420, 3490
- Condon, J. J. 1992, *ARA&A*, 30, 575
- Costagliola, F., Aalto, S., Rodriguez, M. I., et al. 2011, *A&A*, 528, 30
- Dame, T. M., Hartmann, D., & Thaddeus, P. 2001, *ApJ*, 547, 792
- Doherty, R. M., Puxley, P. J., Lumsden, S. L., et al. 1995, *MNRAS*, 277, 577
- Doyon, R., Wright, G. S., & Joseph, R. D. 1994, *ApJ*, 421, 115
- Elmegreen, B. G., Kaufman, M., Bournaud, F., et al. 2016, *ApJ*, 423, 26
- Elmegreen, B. G., Kaufman, M., Struck, C., et al. 2000, *AJ*, 120, 630
- Elmegreen, B. G., Kaufman, M., & Thomasson, M. 1993, *ApJ*, 412, 93
- Elmegreen, B. G., Sundin, M., Kaufman, M., Brinks, E., & Elmegreen, D. M. 1995a, *ApJ*, 453, 139
- Elmegreen, D. M., Elmegreen, B. G., Kaufman, M., et al. 2006, *ApJ*, 642, 158
- Elmegreen, D. M., Elmegreen, B. G., Kaufman, M., et al. 2017, *ApJ*, 841, 43
- Elmegreen, D. M., Kaufman, M., Brinks, E., Elmegreen, B. G., & Sundin, M. 1995b, *ApJ*, 453, 100
- Elmegreen, D. M., Kaufman, M., Elmegreen, B. G., et al. 2001, *AJ*, 121, 182
- Gilbert, A. M., & Grapham, J. R. 2007, *ApJ*, 668, 168
- Herrera, C. N., & Boulanger, F. 2017, *A&A*, 600, A139
- Higdon, J. L. 1995, *ApJ*, 455, 524
- Iffrig, O., & Hennebelle, P. 2017, *A&A*, 604, A70
- Irwin, J. A. 1994, *ApJ*, 429, 618
- Johnson, K. E., & Kobulnicky, H. A. 2003, *ApJ*, 597, 923
- Juneau, S., Narayanan, D. T., Shirley, Y. L., et al. 2009, *ApJ*, 707, 1217
- Kaufman, M., Brinks, E., Elmegreen, B. G., et al. 1999, *AJ*, 118, 1577
- Kaufman, M., Brinks, E., Elmegreen, D. M., et al. 1997, *AJ*, 114, 2323
- Kaufman, M., Grupe, D., Elmegreen, B. G., et al. 2012, *AJ*, 144, 156
- Kepley, A., Leroy, A., Frayer, D., et al. 2014, *ApJL*, 780, L13
- Kobulnicky, H. A., & Johnson, K. E. 1999, *ApJ*, 527, 154
- Krips, M., Neri, R., Garcia-Burillo, S., et al. 2008, *ApJ*, 677, 262
- Madau, P. 1988, *ApJ*, 327, 116
- Martizzi, D., Faucher-Giguere, C.-A., & Quataest, E. 2015, *MNRAS*, 450, 504
- Mengel, S., Lehnert, M. D., Thatte, N., et al. 2002, *A&A*, 383, 137
- Mezger, P. G., & Henderson, A. P. 1967, *ApJ*, 147, 471
- Mineo, S., Rappaport, S., Levine, A., et al. 2014, *ApJ*, 797, 91
- Rosenberg, M. J. F., van der Werf, P. P., & Israel, F. P. 2013, *A&A*, 550, A12
- Rupke, D., Kewley, L., & Chien, L.-H. 2010, *ApJ*, 723, 1255
- Ruszkowski, M., & Begelman, M. C. 2003, *ApJ*, 586, 384
- Scoville, N., Aussel, H., Sheth, K., et al. 2014, *ApJ*, 783, 84
- Shields, J. C. 1993, *ApJ*, 419, 181
- Smith, B. J., Soria, R., Struck, C., et al. 2014, *AJ*, 147, 60
- Smith, B. J., Zaragoza-Cardiel, J., Struck, C., et al. 2016, *AJ*, 151, 63
- Sternberg, A., Hoffmann, T. L., & Pauldrach, W. A. 2003, *ApJ*, 599, 1333
- Struck, C., Kaufman, M., Brinks, E., et al. 2005, *MNRAS*, 364, 69
- Usero, A., Leroy, A. K., Walter, F., et al. 2015, *AJ*, 150, 115
- Vila, M. B., Pedlar, A., Davies, R. D., Hummel, E., & Axon, D. J. 1990, *MNRAS*, 242, 379
- Wetzstein, M., Naab, T., & Burkert, A. 2007, *MNRAS*, 375, 805
- Wild, W., Harris, A., Eckart, A., et al. 1992, *A&A*, 265, 447
- Yang, M., & Phillips, T. 2007, *ApJ*, 662, 284